



Universiteit
Utrecht



Emulating SAI Scenarios in CESM2 and the Effects on the Southern Hemisphere Large-Scale Atmospheric Circulation

MASTER THESIS

Simone Lingbeek
Climate Physics

Supervisors:

Dr. Claudia Wieners
Institute for Marine and Atmospheric research Utrecht (IMAU)

Dr. Michiel Baatsen
Institute for Marine and Atmospheric research Utrecht (IMAU)

Daily supervisor:

Jasper de Jong
Institute for Marine and Atmospheric research Utrecht (IMAU)
July 2024

Abstract

The implementation of adequate and timely policies to prevent the further increase of greenhouse gases in our atmosphere and the most disastrous effects of global warming is becoming increasingly unlikely. In this context, stratospheric aerosol injections (SAI) could provide a solution by (temporarily) decreasing global mean surface temperature. The study of SAI as a climate intervention requires earth system models capable of resolving comprehensive atmospheric chemistry and dynamics. Here we validate a method that makes use of the results of the comprehensive atmospheric model CESM2(WACCM6) to simulate SAI with the simpler CESM2(CAM6). We show that this method is successful in replicating the experiment, reproducing surface temperature and precipitation trends within the range of model-variability. The atmospheric thermodynamical changes caused by SAI are replicated in our model as well, especially for the Southern Hemisphere. We then use our model to conduct experiments with two SAI scenarios - a gradual SAI starting in 2020 and a rapid cooling SAI scenario starting in 2080, both with SSP5-8.5 as background. We study the effects of SAI on the large-scale atmospheric circulation of the Southern Hemisphere. We find that both SAI scenarios are able to prevent the changes in the lower stratosphere observed under SSP5-8.5. In the upper stratosphere SAI leads to a much stronger polar night jet. SAI is also not able to prevent the strong decrease in the frequency of sudden stratospheric warming events as observed under SSP5-8.5. We find a slightly weaker response to SAI in the rapid cooling SAI scenario, but overall trends are identical to the gradual SAI scenario.

Contents

1	Introduction	1
1.1	Climate change and geoengineering	1
1.2	Geoengineering in the Form of Stratospheric Aerosol Injections	1
1.3	General Structure	2
2	Introduction Part I	3
2.1	Previous Research on SAI in Earth System Models	3
2.2	The GLENS Project and Subsequent CESM2 Simulations	3
2.3	Building an Emulator for SAI with CESM2(CAM6)	4
2.4	Scenarios Part I	4
2.5	Research Questions Part I	5
2.6	Results SAI in WACCM	5
3	Introduction Part II	6
3.1	Rapid Cooling with SAI as an Emergency Intervention	6
3.2	Scenarios Part II	6
3.3	The Southern Hemisphere Atmosphere	6
3.3.1	The Subtropical Jet	7
3.3.2	The Eddy-driven Jet	7
3.3.3	The Polar Night Jet	8
3.4	Antarctica and the Southern Hemisphere Atmosphere	8
3.5	Research Questions Part II	9
I	Model Validation	10
4	Methods Part I	10
4.1	Temperature Targets	10
4.2	Using the CESM2(CAM6) Emulator for SAI simulations	10
4.3	Definition of Time Periods for Part I	11
4.4	Vertical Interpolation	11
4.5	Potential Temperature	12
5	Results Part I	13
5.1	Temperature Targets	13
5.2	2-meter Temperature and Precipitation in CAM	13
5.3	SAI 2020 2-meter Temperature Anomalies in CAM and WACCM	14
5.4	SAI 2020 Precipitation Anomalies in CAM and WACCM	16
5.5	SAI 2020 Potential Temperature and Zonal Wind Anomalies in CAM and WACCM	18
6	Discussion Part I	20
II	Southern Hemisphere Atmospheric Circulation	21

7 Methods Part II	21
7.1 Scenarios Used for the Simulations	21
7.2 Definition of Scenarios and Time Periods for Part II	21
7.3 Thermal Wind	22
7.4 Kinetic Energy and Eddy Kinetic Energy	23
7.5 Jet Intensity Maps	23
7.6 Sudden Stratospheric Warmings in Monthly Mean Model Data	24
8 Results Part II	25
8.1 Potential Temperature and Zonal Wind Anomaly	25
8.2 Results Part II: Lower Stratosphere	27
8.2.1 Subtropical Jet	27
8.2.2 Eddy-driven Jet	29
8.3 Results Part II: Upper Stratosphere	33
8.3.1 Polar Night Jet	33
8.3.2 Sudden Stratospheric Warming Events	37
9 Discussion Part II	38
10 Conclusions and Outlook	40
10.1 Part I: Model Validation	40
10.2 Part II: Southern Hemisphere Atmospheric Circulation	40
10.3 Outlook	41
References	46
A Absolute model differences between CAM and WACCM	47
B Potential Temperature and Zonal Wind JJA	48
C 2-meter Temperature in CAM	49
D DJF eddy kinetic energy and Eddy Driven Jet Position	50

List of Acronyms

SRM	Solar radiation management
GMST	Global mean surface temperature
SAI	Stratospheric aerosol injections
STJ	Subtropical jet
EDJ	Eddy-driven jet
PNJ	Polar night jet
SSW	Sudden stratospheric warming event
KE	Kinetic energy
EKE	Eddy kinetic energy

1 Introduction

1.1 Climate change and geoengineering

In the effort of limiting the effects global climate change, eliminating fossil fuels is the most important step to take. Regrettably, the complete elimination of fossil fuels in time to prevent the most disastrous effects of climate change and limit global warming to even 2°C is becoming increasingly unlikely. Even with all currently committed climate action goals, projections show the earth warming significantly above the 1.5°C and 2°C targets from the Paris Agreement (UNFCCC 2023). With this outlook, methods to temporarily lower the earth's global temperature are looked at to buy the global community time to lower atmospheric greenhouse gases. One such method is solar radiation management with stratospheric aerosol injections (SAI).

Geoengineering can be seen as a toolbox of methods that change the earth's climate system to achieve a desired effect. Limiting global mean surface temperature (GMST) increase is the primary goal of geoengineering. The methods of geoengineering can be divided into two basic categories, Carbon Dioxide Removal (CDR) and Solar Radiation Management (SRM) (Shepherd 2009). CDR focuses on lowering the amount of greenhouse gases in the atmosphere, by capturing CO₂ directly or enhancing and facilitating natural processes to speed up the extraction of CO₂ from the atmosphere or oceans. SRM on the other hand focuses on altering the earth's radiation budget. This can be done by increasing the amount of long wave radiation the earth emits into space, for instance with cirrus cloud thinning, but the most widely discussed approach is increasing how much short wave radiation from the sun is reflected back into space, i.e. increasing the planetary albedo. This is done for instance by making deserts more reflective or making clouds brighter like through marine cloud brightening (NAS 2021).

1.2 Geoengineering in the Form of Stratospheric Aerosol Injections

This thesis considers SRM in the form of stratospheric aerosol injections (SAI). Through injection of sulphate aerosols or their precursors at specific points in the stratosphere the earth's radiation budget is changed. At this high altitude the aerosols reflect short wave radiation, lowering the amount of sunlight reaching the earth's surface and subsequently GMST is lowered. It has been argued that SAI is one of the most feasible options for SRM (Lenton and Vaughan 2009; Shepherd 2009).

A direct result of SAI is the absorption of long wave radiation emitted by the earth by the aerosols, resulting in warming in the stratosphere (Ammann et al. 2010). This impacts the global atmospheric circulation patterns and precipitation patterns. It is also important to keep in mind that the effects other than warming caused by increased greenhouse gases are still present in the earth system, for instance ocean acidification will continue if CO₂ concentrations continue to rise. The introduction of sulphate aerosols has unintended consequences too, including in delayed repair of the ozone hole and an increase in acid deposition, and interference with cloud formation.

Eventhough complete understanding of the physical consequences of SAI is not within reach as of now, the physical feasibility in regards to limiting global warming is rather certain. Practically, the succesful deployment of SAI is only possible if the global community can reach consensus on its employment and can ensure no party deploys SAI undemocratically and to the detriment of others. Even then, long-term political and economical stability are crucial, as an abrupt halt would lead to

rapid warming (Robock 2008).

The employment of SAI is not as straight-forward as appears at first glance, and before any decisions can be made about SRM, with SAI or through other means, more research is needed. The National Academy of Sciences made extensive recommendations for solar geoengineering research (NAS 2021), including research into the impacts on atmospheric processes, the climate response, designing a monitoring system, how to govern solar geoengineering activities and ethical considerations for current and future generations.

1.3 General Structure

In this thesis we investigate the climate response to SAI, more specifically the atmospheric dynamics of the Southern Hemisphere. We will use the results from a previous study on SAI conducted with an earth system model with an extensive atmospheric component and comprehensive atmospheric chemistry to build an emulator with a model with a smaller atmospheric component that incorporates no atmospheric chemistry. We do this primarily to save on computation time. We will validate this experiment in Part I, and use it to assess the impact of SAI on the Southern Hemisphere atmospheric circulation in Part II. We will focus on changes in the large scale components of the atmospheric circulation.

The southern hemisphere is of particular interest because of the Antarctic Ice Sheet that is home to a number of tipping points. The triggering of these tipping points can potentially lead to disastrous levels of sea level rise and once these tipping points are reached, there is no way to reverse the effects. Understanding the dynamics of the Southern Hemisphere and the response to SAI is crucial to accurately predict the future evolution of these tipping points and if triggering them can be avoided with the help of SAI.

2 Introduction Part I

2.1 Previous Research on SAI in Earth System Models

Large scale studies on SRM started with the Geoengineering Model Intercomparison Project (GeoMIP) (Kravitz et al. 2011). Experiments reduced the incoming solar radiation either directly or through injection of SO₂ in the stratosphere at one point on the equator, which was then distributed in the atmosphere very quickly by the zonal circulation and on larger time scales the meridional circulation.

It was found that injection of aerosols at just the equator, and uniform solar radiation reduction lead to over-cooling of the tropics and under-cooling of the poles. Kravitz et al. (2016) proposed a different approach, where climate targets were considered the main goal and how to reach those goals through SAI was viewed as a design problem. One set of targets proposed was the global mean surface temperature (T_0), the interhemispheric temperature gradient (T_1) and the pole-to-equator temperature gradient (T_2). The proposed SAI strategy included four injection points, two on each hemisphere, and a feedback algorithm that adjusts the injection rate at those points to achieve the temperature goals. This method was applied by Kravitz et al. (2017) and MacMartin et al. (2017), and then in the Geoengineering Large Ensemble (GLENS) project (Tilmes et al. 2018).

2.2 The GLENS Project and Subsequent CESM2 Simulations

The GLENS project is a 20-member ensemble of gradual SAI simulations. From 2020 onwards SO₂ is injected at four injection points at $\pm 15^\circ\text{N}$ and $\pm 30^\circ\text{N}$ about 5 km above the tropopause. A feedback-control algorithm is used to adjust the injection amounts at each point individually based on the departure of the $T_{0,1,2}$ temperatures defined by Kravitz et al. (2016) from 2020 levels.

The GLENS project was performed using the Community Earth System Model version 1 (CESM1) (Hurrell et al. 2013), with the Whole Atmosphere Community Climate Model (WACCM) as its atmosphere component. This model uses a $0.9^\circ \text{ latitude} \times 1.25^\circ \text{ longitude}$ rectangular grid with 70 vertical layers that reach up to 140 km, or about 10⁻⁶ hPa. It includes comprehensive atmospheric chemistry for the middle atmosphere, incorporating ozone chemistry and chemistry relating to stratospheric sulfate formation. A simpler chemistry scheme is used for the troposphere. Aerosol chemistry is coupled to WACCM through the three-mode version of the Modal Aerosol Module (MAM3).

After the GLENS project the method using four injection points and a feedback algorithm was further explored using the more recent Community Earth System Model version 2, also using a newer version of the WACCM, now version 6 (CESM2(WACCM6)) (Tilmes et al. 2020). WACCM6 has the same horizontal and vertical resolution, but now includes comprehensive chemistry from the troposphere up to the lower thermosphere. The MAM4 modal aerosol scheme is used for the troposphere and stratosphere. We will refer to this model as ‘WACCM’.

Because WACCM is comprehensive in both vertical resolution and atmospheric chemistry, it is well-suited to simulate SAI scenarios. However, due to this it is also a very cumbersome model, requiring more computing time and resources compared to less comprehensive models. This limits its use in ensemble studies and studies considering a large range of scenarios. Computational cost also limits its use for simulations with a longer timeseries at higher resolution, required to study smaller scale phenomena like tropical cyclones.

2.3 Building an Emulator for SAI with CESM2(CAM6)

Reducing the amount of computing resources needed for an experiment can be done by using a smaller, less comprehensive model and using previous results from WACCM as external forcing to the model, essentially building an emulator. Pflüger et al. (2024) introduce a method for building such an emulator of WACCM to model SAI. They use the same CESM2 model configuration is used as in Tilmes et al. (2020), but the Community Atmosphere Model version 6 (CAM6) is used for the atmosphere component (Danabasoglu et al. 2020). This model has only 32 vertical levels and no atmospheric chemistry. We will refer to this model as ‘CAM’. The aerosol field established in the WACCM simulation is used as an external forcing. To maintain 2020 levels of GMST, the necessary globally averaged aerosol optical depth (AOD) field is found through the same feedforward-feedback algorithm. All other forcing fields are then scaled accordingly. In contrast to the WACCM simulations, the temperature gradients T_1 and T_2 are not adjusted for.

The WACCM SAI experiment is well-suited to build an emulator for, as the employment of SAI is used as a means to reach a climatic goal. It prescribes an aerosol burden in response to model behaviour, in stead of gauging the model response to a certain aerosol burden. This removes the amount of SO_2 injected into the stratosphere from the experiment design and allows for translation of the aerosol distribution to another model that might respond differently to the introduction of aerosols.

2.4 Scenarios Part I

There are two simulations performed with CAM and WACCM. The first simulation follows the historical spin-up and is continued by the SSP5-8.5 scenario (Riahi et al. 2007). The second simulation branches from the first simulation in 2020 and from then on introduces SAI to stabilise temperatures using the SSP5-8.5 scenario as background. Here we will refer to it as the gradual SAI scenario. A schematic view of the GMST response in each scenario is shown in Figure 1.

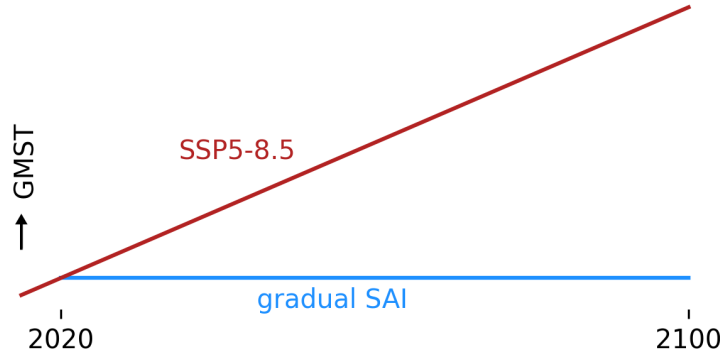


Figure 1: Schematic of the global mean surface temperature in the two scenarios used in Part I, the SSP5-8.5 and gradual SAI scenarios.

2.5 Research Questions Part I

The first part of this thesis is the validation of this method and model in its use as an emulator, simulating SAI scenarios based on the WACCM results. Two experiments, a high-warming scenario and a gradual SAI scenario, are used to assess the impact of SAI in each model (CAM and WACCM). We calculate the three temperature targets for all models and we will look at the model results for 2-meter temperature for additional insight into the performance of CAM in regards to regulating surface temperatures. We discuss both annual and seasonal patterns. Additionally, we discuss precipitation patterns.

The most important difference in dynamics between the two models lies in the inclusion of ozone chemistry and thus the interaction of stratospheric aerosols and ozone. It is known that sulphate aerosols in the stratosphere accelerate chemical ozone loss through halogen activation and strengthening of the polar vortex (Bednarz et al. 2023c). CAM does not include this process, and assessing whether the dynamical response to SAI is comparable to WACCM is thus important. To this end we assess any differences in the vertical profile between the two models, we compare the zonally averaged potential temperature and zonal winds.

We formulate the following research questions for Part I:

When applying the stratospheric aerosol emulator to a gradual SAI scenario in CESM2(CAM6), are we able to reproduce from Tilmes et al. (2020)

- i the temperature targets T_0 , T_1 and T_2 ?*
- ii the spatial and seasonal variations of temperature, precipitation and general aspects of the atmospheric circulation?*

2.6 Results SAI in WACCM

The experiments performed with WACCM (Tilmes et al. 2020) showed that surface temperatures were generally controlled with SAI. Under SAI the tropics warmed slightly, the mid-latitudes cooled slightly and the poles warmed slightly as well. Zonal mean precipitation showed an increase in the tropics and a decrease or no significant change everywhere else. An apparent warming hole over the Northern Atlantic was observed in all simulations and was likely related to observed changes in the Atlantic Meridional Overturning Circulation. No changes in seasonal patterns were discussed, nor were changes in potential temperature and atmospheric circulation.

3 Introduction Part II

3.1 Rapid Cooling with SAI as an Emergency Intervention

As sufficient climate policies to prevent global warming of 1.5°C or even 2°C (UNFCCC 2023), it is unlikely the global community will implement a proactive gradual SAI scenario in time as well. Employing SAI much later on after prolonged heating of the climate system is a realistic, more reactive, scenario. The earth could be cooled very rapidly, allowing the end-of-century GMST goals to be reached after the climate system has endured an even longer period of warming than it has to date. The effects of such an intervention are largely uncertain. While it is rather certain that SAI could lower GMST, it is not certain what effects of previous warming can be reversed, if at all. The SAI 2080 scenario introduced in Pflüger et al. (2024) is such a scenario, SAI is employed from 2080 onwards to achieve rapid cooling to 2020 levels.

3.2 Scenarios Part II

For the second part of this thesis we consider the two CAM simulations from Part I, the SSP5-8.5 and the gradual SAI simulations, and the SAI 2080 scenario from Pflüger et al. (2024). We will refer to this simulation as the rapid cooling SAI simulation. The rapid cooling simulation is branched from the SSP5-8.5 simulation in 2080, SAI is then deployed to restore T_0 to 2020 levels. The control algorithm is adjusted up to the first six years to prevent extremely high aerosol concentrations that would result in too rapid cooling. A schematic view of the GMST response for this scenario is shown in Figure 2.

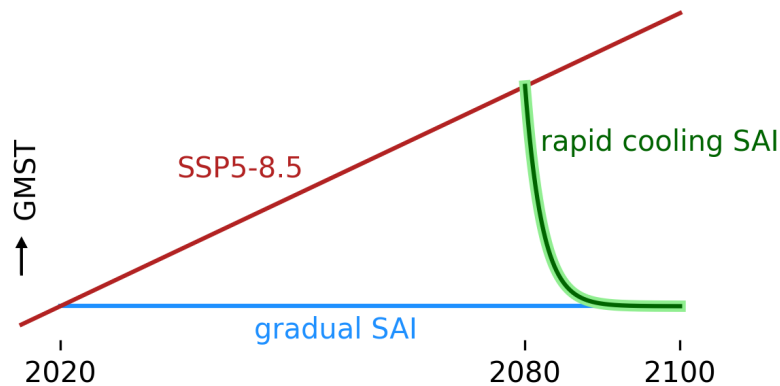


Figure 2: Schematic of the global mean surface temperature in the two scenarios used in Part I, the SSP5-8.5, the gradual SAI and the rapid cooling SAI scenarios.

3.3 The Southern Hemisphere Atmosphere

The atmosphere is home to a number of large scale circulation phenomena. Though the two hemispheres are symmetrical in the occurrence of these phenomena, the exact location, frequency of occurrence and other behaviour of these phenomena differs between the two hemispheres. The Southern Hemisphere circulation is generally more stable than its counterpart in the Northern Hemisphere. In this thesis we focus on three so-called jets, large scale circulation phenomena that

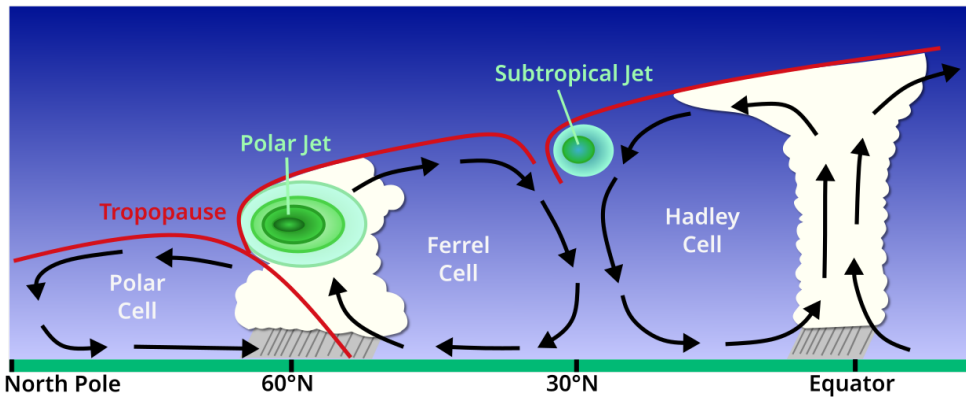


Figure 3: Cross section of the Northern Hemisphere atmospheric circulation, with the subtropical jet and polar jet (or eddy-driven jet) in relation to the circulation cells. Image by: Original: National Weather Service, JetStream Vector: Sleske - Own work based on: Jetcrosssection.jpg, CC BY-SA 4.0, <https://commons.wikimedia.org/w/index.php?curid=75169357>

persist throughout the year or in a specific season. We discuss the subtropical jet and the the eddy-driven jet in the lower stratosphere (up to 50 hPa), and the polar night jet in the upper stratosphere (above 50 hPa).

3.3.1 The Subtropical Jet

The subtropical jet (STJ) forms at the convergence of the upper branches of the Hadley and Ferrel cells in the lower stratosphere, with a maximum around 200 hPa, see Figure 3 (the Southern Hemisphere is analogous to the Northern Hemisphere). Influenced by the Coriolis force westerly winds form here, the magnitude of which is determined by the temperature gradient below the convergence zone (Zolotov et al. 2018). The STJ occurs year-round but is strongest in winter, in tandem with the stronger winter Hadley cell, where it is located around 30°S.

In the past decades, the southern hemisphere STJ has been observed to shift poleward and slightly decrease in wind speed, though not significant (Zolotov et al. 2018). The STJ was also observed to be increasingly wavy (Martin and Norton 2023). Under high global warming the STJ is projected to shift further poleward and increase in strength (Chenoli et al. 2017).

Simulations with SAI at singular injection points showed a small but significant decrease in the strength of the STJ (Richter et al. 2017). From historical simulations it has been argued as well that anthropogenic aerosols contribute to deceleration (Wang et al. 2020).

3.3.2 The Eddy-driven Jet

At the divergence of the upper branches of the Ferrel and Polar cells another jet forms, the polar jet in Figure 3. This jet is at a lower altitude and stronger than the STJ. However, it is also much wavier than the STJ (Martin and Norton 2023). Because of this, and to avoid confusion with the polar night jet, we will refer to this jet as the eddy-driven jet (EDJ).

The EDJ has been observed to become increasingly wavy in the past decades, also shifting poleward, even more strongly than the STJ, but no significant trend in the wind speed was observed

(Martin and Norton 2023). Under high global warming the EDJ is projected to shift further poleward (Curtis et al. 2020).

It is not certain how the EDJ will respond under SAI, though it has been shown that the EDJ is influenced by the strength of the polar night jet in the upper stratosphere, where a strengthened jet leads to a poleward shift of the EDJ (Kidston et al. 2015). Any changes in the polar night jet due to SAI are thus likely to cause changes in the EDJ as well.

3.3.3 The Polar Night Jet

The polar night jet (PNJ) forms in the upper stratosphere during winter in response to the large equator-to-pole meridional temperature gradient. The pole becomes encircled with a belt of strong westerly winds in the upper parts of the stratosphere, above ≈ 50 hPa at around 60° S (Lee 2021).

With high warming the PNJ is projected to increase in strength, most notably in late SH spring, effectively delaying the ultimate breakdown of the PNJ (Ceppi and Shepherd 2019).

The warming in the lower stratosphere due to SAI leads to an increase of the equator-to-pole meridional temperature gradient, causing increasing zonal winds via the thermal wind balance. This effect is strongest in the late winter/early spring (Bednarz et al. 2023a; Bednarz et al. 2023c).

When disturbances near the surface propagate to the stratosphere, the PNJ can suddenly weaken, leading to a sudden increase in temperatures of the polar stratosphere and sometimes a complete breakdown of the jet. These events are called sudden stratospheric warming events (SSWs) and occur very rarely in the Southern Hemisphere in the current climate. Their frequency is projected to strongly decrease with increasing global warming (Jucker et al. 2021).

3.4 Antarctica and the Southern Hemisphere Atmosphere

The high-latitude Southern Hemisphere is of particular interest in the context of climate change and the prevention of it. The Antarctic Ice Sheet (AIS) could contribute greatly to global sea level rise if it were to become unstable under global warming. Observed instabilities of the West-Antarctic Ice Sheet (WAIS) alone could contribute to significant sea level rise (IPCC 2021).

Large scale atmospheric dynamical changes affect the Antarctic ice sheet, changes in temperature, precipitation and wind fields alter the surface mass balance of the ice sheet. More distantly dynamical changes affect the ice sheet through changes in the ocean, mainly in the rate and location of overturning circulations. A warmer ocean together with a warmer atmosphere can lead to the loss of ice shelves (Wang et al. 2023) and their disappearance has been observed to increase the flow of glaciers feeding into the ocean (Scambos et al. 2004), contributing to mass loss of the AIS.

The Southern Hemisphere high stratosphere has low variability in the current climate, but any changes could have far-reaching effects on the surface climate. It has been observed that SH stratospheric polar vortex weakening contributes to climate anomalies in Australia and New Zealand, southeast Africa and southern South America. Additionally, the wind stress over the ocean around Antarctica is weakened and the Ross and Amundsen seas experience warmer climate (Domeisen and Butler 2020). There is thus a clear interaction between the atmospheric dynamics and local climate in the Southern Hemisphere.

The effect of SAI on the Antarctic ice sheet has been studied by McCusker et al. (2015), who found that a rapid introduction of sulphate aerosols in the stratosphere could not prevent the collapse of the WAIS. Sutter et al. (2023) found similar results. However, both studies use very simple aerosol

schemes, that for instance only inject aerosols in the tropics. These types of schemes are known to lead to over-cooling of the tropics and under-cooling of the poles. As stated before, the studies using a feedback-control algorithm to maintain the $T_{0,1,2}$ temperature targets were largely successful in this regard.

3.5 Research Questions Part II

In the second part of this thesis the effect of SAI on the high-latitude Southern Hemisphere atmospheric dynamics is investigated, both in the gradual and rapid cooling scenarios. The focus here lies on large scale circulation patterns, as they largely dictate local climate in the Southern Hemisphere.

We formulate the following research questions for Part II:

What are the impacts of the gradual SAI scenario on the Southern Hemisphere

i subtropical and eddy-driven jets in the lower stratosphere?

ii polar night jet and sudden stratospheric warming events in the upper stratosphere?

How do the results for i and ii change under the rapid cooling SAI scenario?

Part I

Model Validation

4 Methods Part I

4.1 Temperature Targets

The WACCM simulations use the feedback algorithm to maintain three temperature targets in their SAI scenario. These temperature targets are defined in Kravitz et al. (2016) as the projection of $T(\psi)$ onto the first three components of the Legendre polynomial expansion of $\sin(\psi)$,

$$\begin{aligned} T_0 &= \frac{1}{2} \int_{-\pi/2}^{\pi/2} T(\psi) \cos(\psi) d\psi, \\ T_1 &= \frac{1}{2} \int_{-\pi/2}^{\pi/2} T(\psi) \sin(\psi) \cos(\psi) d\psi, \\ T_2 &= \frac{1}{2} \int_{-\pi/2}^{\pi/2} T(\psi) \frac{1}{2}(2 \sin^2(\psi) - 1) \cos(\psi) d\psi, \end{aligned} \quad (1)$$

where ψ is latitude, $T(\psi)$ is the zonal-mean temperature for each latitude.

The T_0 temperature target translates to global mean surface temperature (GMST), the T_1 is interpreted as the inter-hemispheric temperature gradient and T_2 is interpreted as the equator-to-pole temperature gradient. From the model output these temperature targets can be evaluated using Eq. 1.

4.2 Using the CESM2(CAM6) Emulator for SAI simulations

The emulator for SAI simulations is introduced in Pflüger et al. (2024), it implements SAI via prescribed aerosol fields, as opposed to sulphate injections that result in aerosol fields through model physics. As per Pflüger et al. (2024), the protocol works as follows:

- Every year, observe the deviation of GMST from the target.
- Based on past GMST deviations, infer the level of SAI - expressed in terms of global mean aerosol optical depth (AOD) - which is necessary to achieve the desired target.
- Use the AOD to scale all SAI-related aerosol fields appropriately.
- Feed the scaled fields into CAM6.

The first two steps are implemented via the feedforward-feedback control algorithm as established in Kravitz et al. (2017). The control algorithm stabilises only GMST, not inter-hemispheric and equator-to-pole temperature gradients from section 4.1.

The prescribed fields are the averaged fields from the WACCM simulation, this simulation is called the *Geo SSP5-8.5 1.5 scenario* in Tilmes et al. (2020). The fields are normalised, averaged and fit, to then arrive at an amplitude for each component. The total SO₄ concentration from WACCM in 2100 at each latitude and model layer is shown in Figure 4. The highest concentration of aerosols is found around the four injection points (15°N/S and 30°N/S), concentrations remain higher around the equator and diminish towards the poles. Concentrations in the Southern Hemisphere are higher than in the Northern Hemisphere.

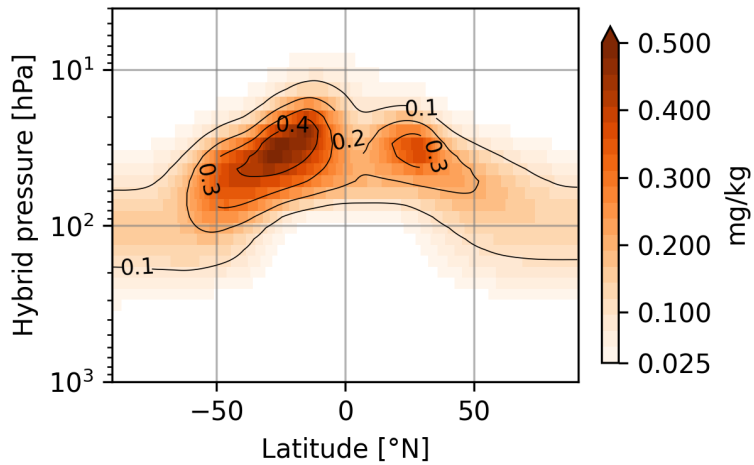


Figure 4: Total SO₄ concentration from WACCM in 2100.

4.3 Definition of Time Periods for Part I

Throughout this first part, three time periods are selected to visualise and interpret the results from the simulations. For each period the 20-year mean is taken, unless specified otherwise. These periods are defined as follows:

- **Reference** The period 2016-2035 of the SSP5-8.5 simulation.
- **Control** The period 2080-2099 of the SSP5-8.5 simulation.
- **SAI 2020** The period 2080-2099 of the gradual SAI simulation.

4.4 Vertical Interpolation

The atmospheric vertical levels of CESM are defined at hybrid pressure coordinates. However, for ease of computation and visualisation, conversion to pressure coordinates is preferred. The hybrid pressure coordinates are converted to pressure coordinates for each timestep at each gridpoint. Then a logarithmic interpolation scheme is used to project the model output onto uniform constant pressure coordinates. For a variable f at pressure coordinate p the scheme takes the form

$$f = \frac{f_1 - f_0}{\ln \frac{p_1}{p_0}} \cdot \ln \frac{p}{p_1} + f_0, \quad (2)$$

where f_0, p_0 are the variable and pressure at the lowest model level and f_1, p_1 are the variable and pressure at the first model level above f, p . For CAM the model output is converted from 32 to 34 pressure levels ranging from 3.5 to 993 hPa. We add two levels in the upper stratosphere, compared to the model output, for ease of analysis in this region. For WACCM the SSP5-8.5 model output was published in pressure levels, 19 pressure levels ranging from 1 to 1000 hPa. The WACCM gradual SAI scenario model output is converted from 70 to those same 19 pressure levels to enable direct comparison.

No interpolation is needed of the horizontal grids as these are identical in all models.

4.5 Potential Temperature

With the vertical coordinate converted to pressure coordinates, the potential temperature θ is calculated through

$$\theta = T \left(\frac{p_{ref}}{p} \right)^\kappa, \quad (3)$$

where T is the air temperature, $p_{ref} = 1000$ hPa is the reference pressure, p is the pressure. κ is the ratio $\frac{c_p - c_v}{c_p}$, with $c_p = 1004 \text{ J kg}^{-1} \text{ K}^{-1}$ the specific heat of an ideal gas at constant pressure and $c_v = 717 \text{ J kg}^{-1} \text{ K}^{-1}$ that at constant volume.

5 Results Part I

This section contains the results of the comparison between the CAM and WACCM simulations.

5.1 Temperature Targets

The deviations from the temperature targets in Eq. 1 were calculated from 2-meter temperature for all simulations. The results are shown in Figure 5. The results from the SSP5-8.5 simulations with CAM and WACCM are near identical for T_0 , showing comparable variability and arriving at virtually the same final GMST. The results from the gradual SAI simulations are also comparable, both simulations succeeding in maintaining 2020 GMST levels with comparable variability.

Deviations from T_1 and T_2 are again comparable in CAM and WACCM. The SSP5-8.5 simulation in CAM arrives at a deviation from T_1 about 25% lower than in WACCM. Trendline analysis (not shown) confirms that the increase in ΔT_1 in CAM is about 30% lower than in WACCM. The trend in ΔT_2 is about 20% lower in CAM than in WACCM. Though significant, qualitatively the behaviour of CAM is very similar to that of WACCM and the difference can be attributed to individual model response. The gradual SAI simulation in CAM is comparable to WACCM, maintaining T_1 and T_2 with similar variability and no significant trend in either model.

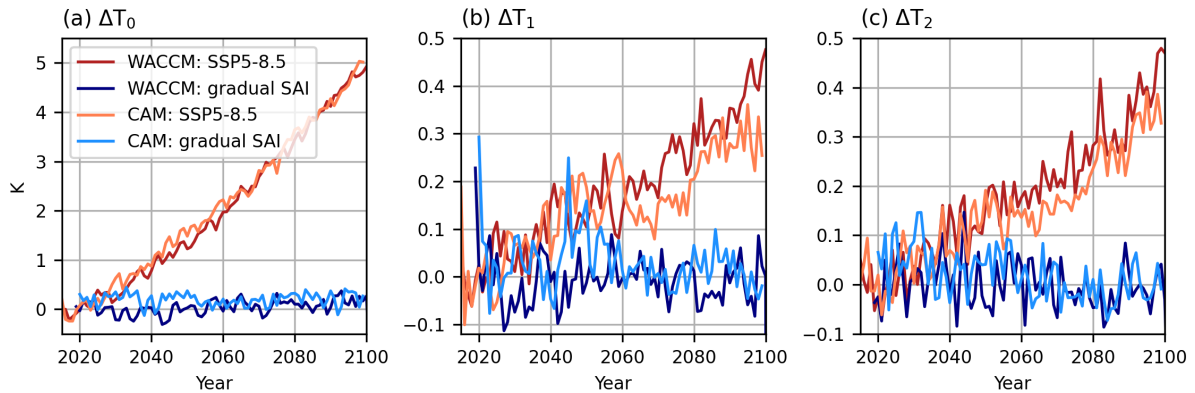


Figure 5: Deviations from temperature targets T_0 , T_1 , T_2 as compared to 2016-2025 mean, for the SSP5-8.5 and gradual SAI scenarios in CAM and WACCM.

5.2 2-meter Temperature and Precipitation in CAM

Figure 6 shows the Reference 2-meter temperature and precipitation, their anomalies for Control compared to the Reference and their anomalies for SAI 2020 compared to Control. In Figure 6(b) the Control period shows expected warming patterns, with the land area warming more than the sea and the poles warming more relatively due to polar amplification. Anomalous warming off the coast of Antarctica and in the Arctic Ocean indicates a retreat of sea-ice at both poles. The anomalous warming over the eastern Pacific ocean resembles the spatial sea surface temperature pattern of El Niño. The slight cooling over the northern Atlantic ocean resembles a North Atlantic warming hole, generally attributed to changes in ocean heat transport and weakening of the Atlantic meridional overturning circulation (AMOC) but also atmospheric circulation changes due to anthropogenic forcing (Menary and Wood 2018; He et al. 2022).

The SAI 2020 anomaly compared to the Control, shown in Figure 6(c), shows that SAI is able to compensate for most of the warming in Control. The land area is cooled more than the sea, as are the poles. Sea-ice retreat is largely prevented in both the Arctic and the Antarctic. The anomalous warming over the eastern Pacific ocean is not prevented, as is the North Atlantic warming hole.

The precipitation anomaly in Control, shown in Figure 6(e), shows a general increase in precipitation. Most significant drying can be attributed to a shift in the intertropical convergence zone (ITCZ), with a southward shift over the Atlantic and eastern Pacific Ocean, expected patterns under increased anthropogenic forcing (Mamalakis et al. 2021). The shift over the eastern Pacific Ocean is possibly related to the El Niño-like warming observed in Fig. 6(b). No significant shift or other change in ITCZ is observed over the Indian and western Pacific Ocean.

In Figure 6(f) the precipitation anomaly of SAI 2020 compared to Control shows opposite trends, apparently preventing most increase in precipitation. The southward shift of the ITCZ is mostly prevented, though not entirely over the eastern Pacific.

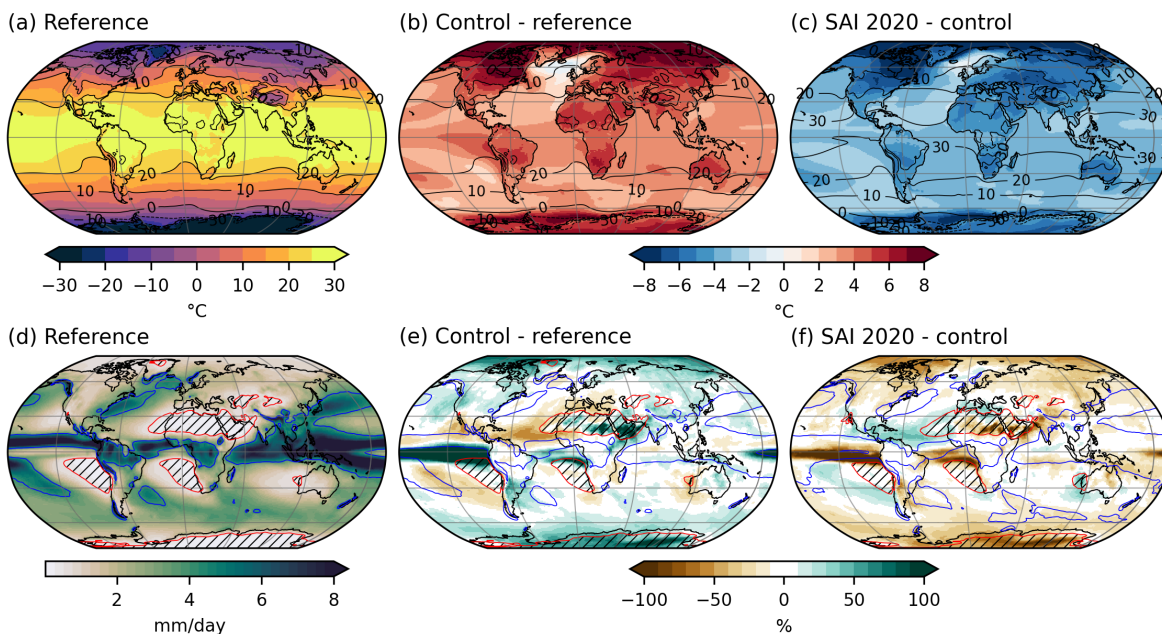


Figure 6: CAM model results; (a): Reference annual mean 2-meter temperature with contours in 10°C intervals; (b): Annual mean 2-meter temperature anomaly for Control compared to Reference, Reference shown in black contours in 10°C intervals; (c): Annual mean 2-meter temperature anomaly for SAI 2020 compared to Control, contours as in (b) but for Control; (d): Reference annual mean precipitation in mm/day, 4 mm/day shown in blue contours, < 0.3mm/day shown in red contours with hatching; (e) Annual mean precipitation anomaly for Control compared to Reference, contours as in (d); (f): Annual mean precipitation anomaly for SAI 2020 compared to Control, contours as in (d) but for Control.

5.3 SAI 2020 2-meter Temperature Anomalies in CAM and WACCM

The annual and seasonal mean 2-meter temperature anomalies of SAI 2020 compared to the Reference for CAM and WACCM are shown in Figure 7. Figure 7(c) shows the difference between

(a) and (b), i.e. the inter-model difference corrected for their difference in SAI 2020. Figures 7(f) and (i) show the annual and seasonal zonal mean anomalies for CAM and WACCM respectively.

The annual mean anomalies in Figures 7(a) and (b) show a generally similar pattern of warming over the tropics, cooling over the subtropics and warming over the poles. The Arctic warms more in CAM than it does in WACCM, at most 3°C. Both models show significant cooling over the northern Atlantic Ocean, again resembling the North Atlantic warming hole seen in Figure 6, CAM more so than WACCM. The El Niño pattern in the eastern Atlantic is visible in both models, though more pronounced in CAM.

Figure 7(c) confirms the patterns described above. The figure also highlights the difference in response over North America and off the coast of Antarctica between 0° and 30°E, where CAM slightly cools and WACCM slightly warms, leading to a significant difference.

In Figures 7(d) and (e), the seasonal response of CAM is shown. Comparison between the two seasons and the annual mean shows that most warming at the poles occurs during their respective winter. This is further confirmed by the zonal mean anomaly in Figure 7(f). The El Niño-like pattern in the eastern Pacific Ocean is stronger in magnitude in JJA, though more expansive in DJF, though neither anomaly shows up in the zonal mean anomaly figure.

The same patterns as in the annual mean are visible in Figures 7(g) and (h), with the Antarctic as a whole warming in the Southern Hemisphere winter and the Barentsz sea in the Arctic warming significantly in the Northern Hemisphere winter. This pattern is confirmed by Figure 7(i).

The differing response between the two models in the Arctic and Antarctic temperatures is possibly a result of model-specific sensitivity to cloud feedbacks, which are known to be one the greatest sources of uncertainty in climate modeling (Schneider et al. 2017).

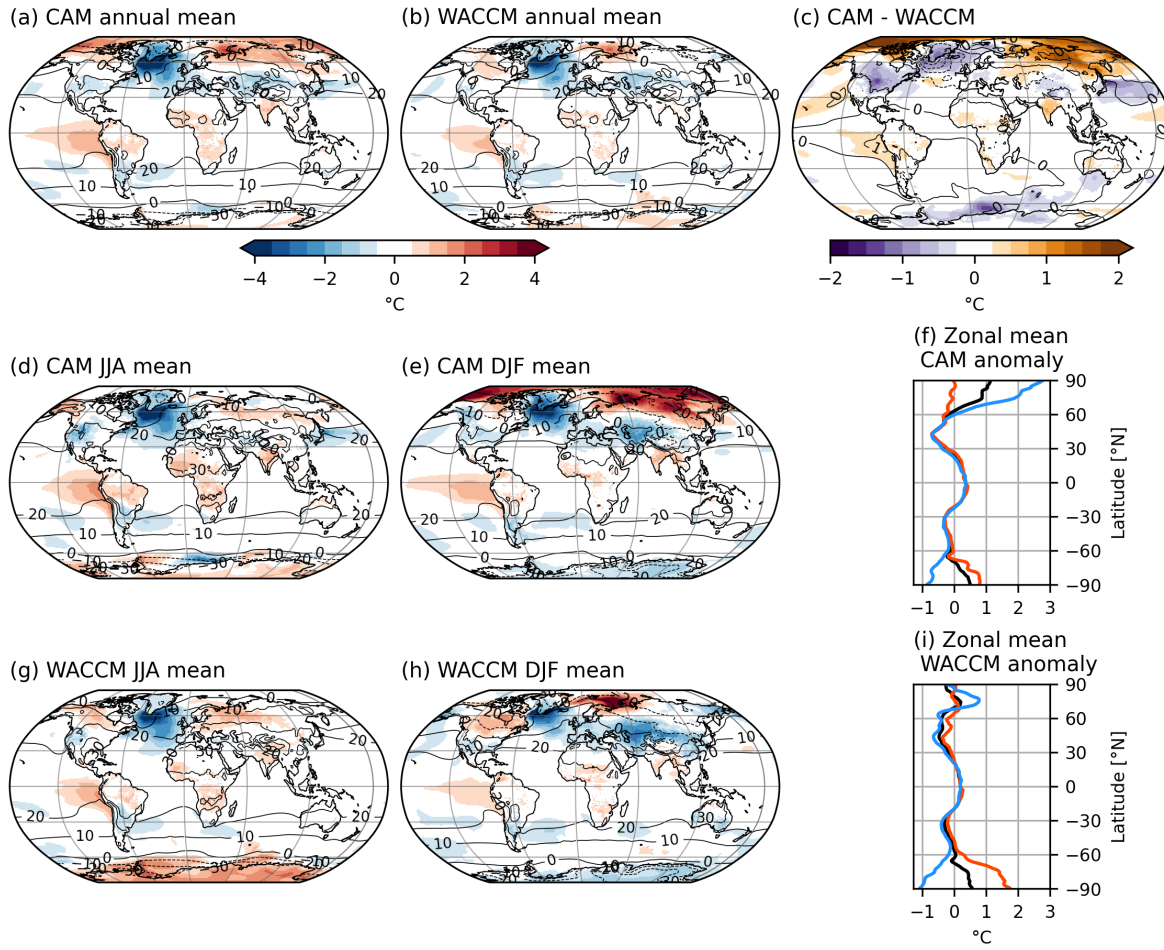


Figure 7: (a,b): Annual mean 2-meter temperature anomalies of SAI 2020 compared to Reference in (a) CAM and (b) WACCM. Reference mean temperature shown in black contours in 10°C intervals; (c): Difference between CAM and WACCM temperature anomalies. WACCM anomaly shown in black contours in 1°C intervals; (d,e): CAM 2-meter temperature anomalies as in (a,b) for (d) JJA and (e) DJF; (f): CAM zonal average 2-meter temperature anomaly as in (a,d,e), annual mean anomaly in black, JJA anomaly in red, DJF anomaly in blue; (g,h,i): analogous to (d,e,f) for WACCM.

5.4 SAI 2020 Precipitation Anomalies in CAM and WACCM

The annual and seasonal mean precipitation anomalies of SAI 2020 compared to Reference for CAM and WACCM are shown in Figure 8. Figure 8(c) shows the difference between (a) and (b) as above in Figure 7, note that this difference is given in percentage points. Figures 8(f) and (i) show the annual and seasonal zonal mean anomalies for CAM and WACCM respectively.

The annual mean anomalies in Figures 8(a) and (b) show a similar pattern overall, with a small decrease in precipitation over most of the globe and larger increase in drier areas and the tropical oceans. CAM shows a much larger precipitation increase over the eastern Pacific Ocean, with a southward shift of the ITCZ. This shift is possibly correlated with the observed anomalous warming in the region (see Figure 7). Contrastingly WACCM shows a larger increase than CAM over dry

areas like the Arabian Peninsula.

The same patterns are observed in the seasonal precipitation anomalies in Figures 8(d), (e), (g) and (h), with the exception of southern Brazil, where CAM shows a larger increase than WACCM in the JJA mean. The zonal mean anomalies in Figures 8(f) and (i) confirm the observed trends further, showing that precipitation in the ITCZ increases twice as much in CAM compared to WACCM, as does precipitation in the Arctic. The Antarctic shows the opposite trend, getting more wet in WACCM than in CAM.

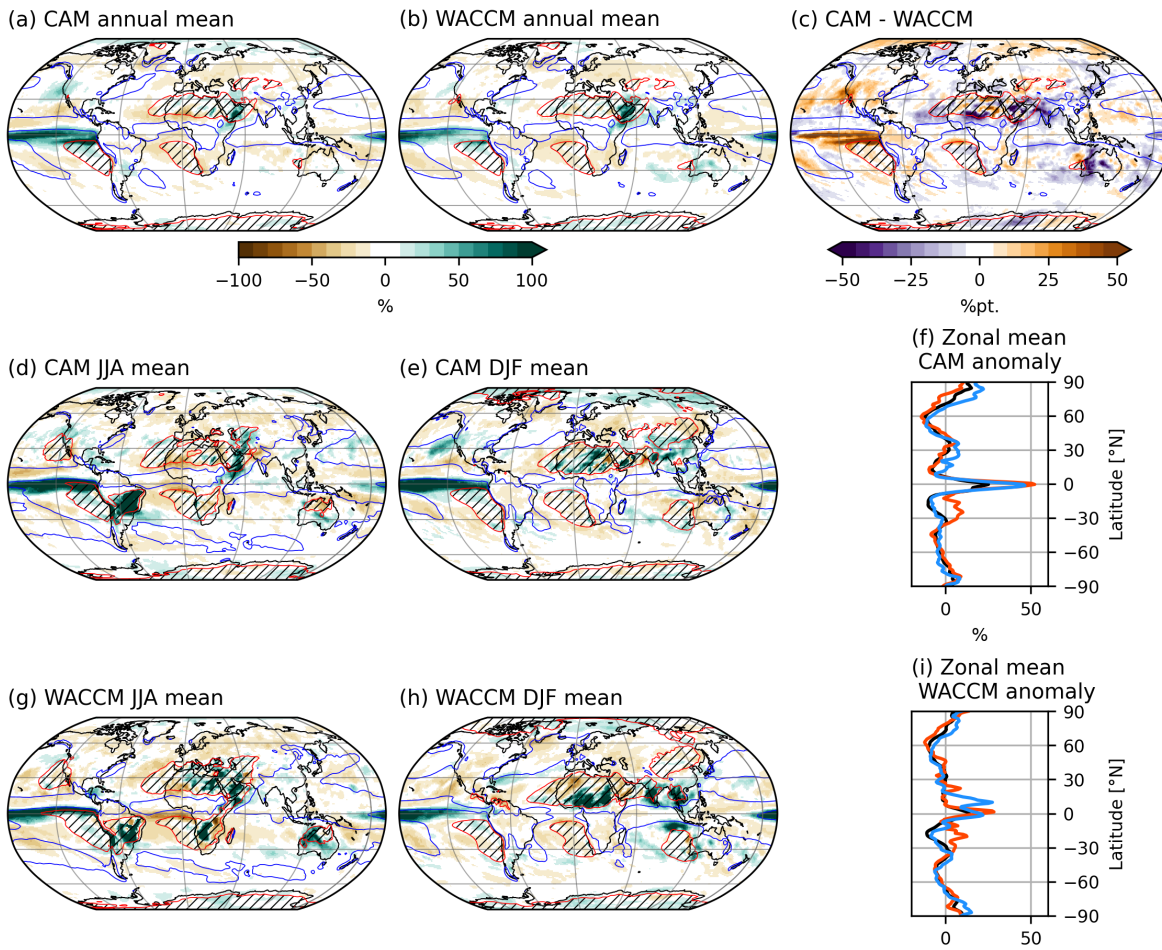


Figure 8: (a,b): Annual mean precipitation anomalies of SAI 2020 compared to Reference in (a) CAM and (b) WACCM. Reference mean precipitation shown, 4 mm/day in blue, < 0.3mm/day in red with hatching; (c): Difference between CAM and WACCM precipitation anomalies. WACCM Control mean precipitation as in (b); (d,e): CAM anomalies as in (a,b) for (d) JJA and (e) DJF; (f): CAM zonal average precipitation anomaly as in, annual mean anomaly in black, JJA anomaly in red, DJF anomaly in blue; (g,h,i): analogous to (d,e,f) for WACCM.

5.5 SAI 2020 Potential Temperature and Zonal Wind Anomalies in CAM and WACCM

The zonal mean potential temperature θ anomaly and the zonal mean zonal wind anomaly for CAM and WACCM are shown in Figure 9, for both the annual and seasonal means. In Figures 9(a)-(f) the potential temperature anomaly shows significant warming in the stratosphere, in a pattern reminiscent of the aerosol field from Figure 4. Concentrated around 15°N/S and 30°N/S , around 50 hPa in the stratosphere, and around the equator. The warming extends to the poles only in the summer hemisphere, due to the poles receiving little to no radiation during the polar night in their respective winter.

The cooling observed in CAM over the Arctic in winter is not observed in WACCM at the same magnitude, any cooling extends to about the same altitude, but is not as severe as it is in CAM. CAM also shows more cooling than WACCM in the Antarctic winter, though the difference is not as stark as in the Arctic. The cooling effect of greenhouse gases in the upper stratosphere is visible in CAM and WACCM in the annual and seasonal means. There is no significant potential temperature change observed below about 300 hPa.

The zonal mean zonal wind anomaly in Figures 9(g)-(l) shows a large increase in zonal winds in the upper stratosphere in both hemispheres. The seasonal mean figures reveal that most zonal wind increase occurs in the winter hemisphere. The polar night jet (PNJ) forms in the upper stratosphere in winter, driven by the large latitudinal temperature gradient in the lower stratosphere during the polar night. The maximum increase in wind speed is observed above the area with the largest increase in the latitudinal temperature gradient, around 60°N/S in the respective winter. See Figures 9(b), (c), (e) and (f), discussed above. The largest anomaly is visible on the equator side of the PNJ in the upper stratosphere, indicating an increase in strength and an equatorward shift. This pattern is observed everywhere, except in the Arctic winter in WACCM (Fig. 9(l)). There the PNJ only increases in strength slightly, correlating to the temperature anomaly (Fig. 9(f)).

In the upper stratosphere over the equator the easterly winds increase in both models, though WACCM also shows increased westerly winds in this region. The temperature response does not fully explain this anomaly in WACCM. Similar responses have been observed by Bednarz et al. (2023b) in simulations with SAI over the equator.

Lower stratospheric and tropospheric winds are largely unchanged in both CAM and WACCM, with the anomaly remaining smaller than 2 m/s (white area). This correlates with the insignificant temperature changes observed in Figures 9

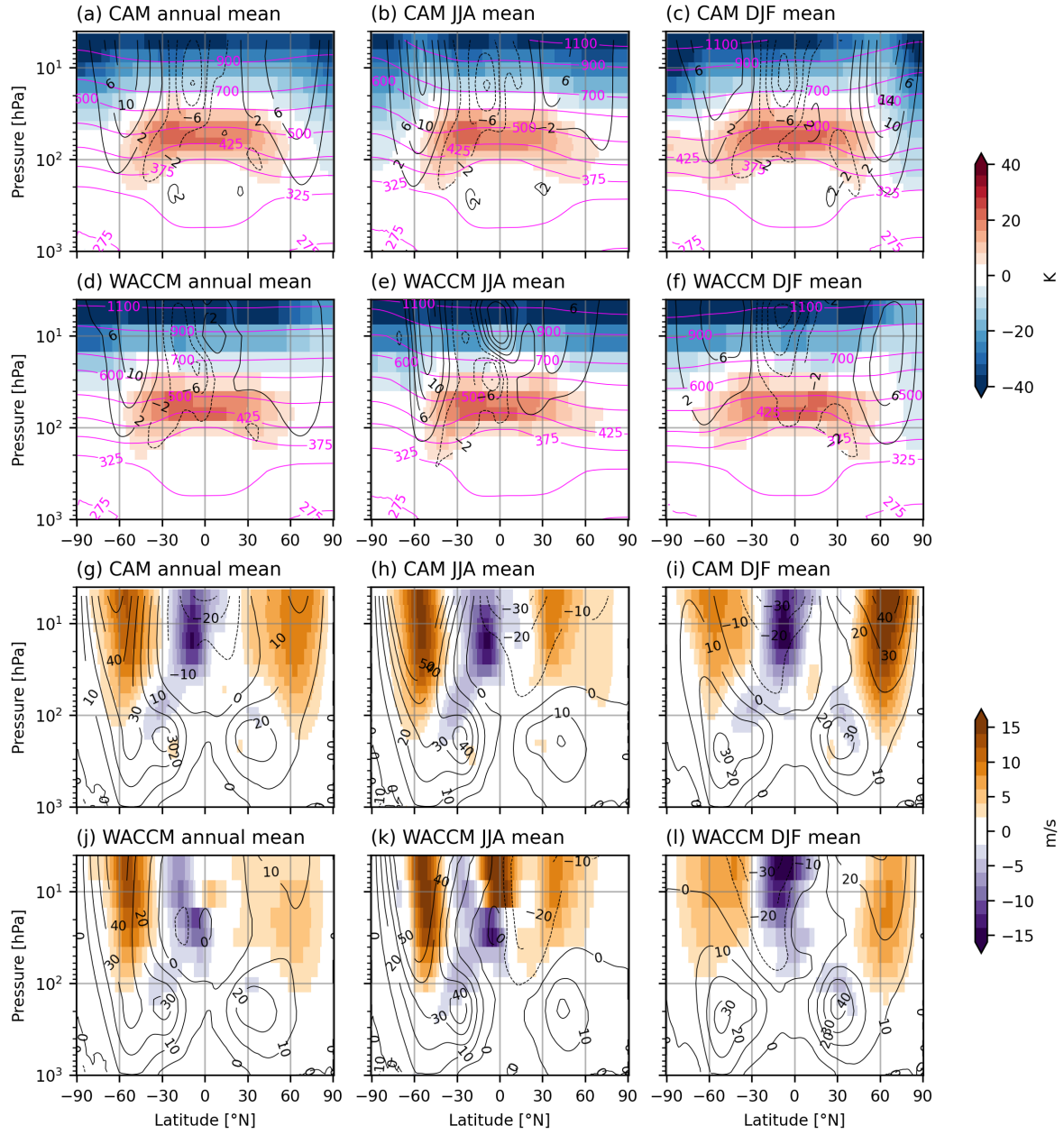


Figure 9: (a-f): Zonal mean potential temperature anomaly of SAI 2020 compared to Reference for (a-c) CAM and (d-f) WACCM, annual, JJA and DJF mean shown for both models. Reference potential temperature shown in magenta contours, zonal mean zonal wind anomalies shown in black contours; (g-l): Zonal mean zonal wind anomaly of SAI 2020 compared to Reference for WACCM and CAM analogous to (a-f), Reference zonal wind shown in black contours.

6 Discussion Part I

As a model for SAI in a high-warming scenario, CAM performs objectively well. GMST is maintained at 2020 levels as expected and most effects of global warming are prevented in proportion; land and polar oceans warm more under high global warming and CAM is generally able to prevent this trend from emerging. The same can be said about precipitation trends, though not as decisively. The general wetting under high global warming is mostly prevented with SAI.

In comparison to WACCM the SAI emulator with CAM is able to reproduce the behaviour of the temperatures T_0, T_1, T_2 . Though the CAM response to the SSP5-8.5 scenario differs from WACCM, our analysis shows it is possible to maintain the temperature targets with the emulator with similar variability as WACCM. However, analysis of global surface temperature patterns shows that large differences in the response to SAI are still present, most prominently in the modelling of polar climate. This highlights the limitations to the use of the temperature targets as a metric by which to measure the success of an SAI strategy. If the goal is to create a uniformly effective SAI strategy with little to no regional bias, T_0, T_1, T_2 are not sufficient metrics.

Differences in model response are apparent for both temperature and precipitation, with the latter showing the most significant differences. However, we must emphasise that this difference is relatively small when compared to the absolute differences between the two models. In Appendix A the absolute difference between CAM and WACCM is shown for temperature and precipitation. CAM is clearly biased towards a warmer Northern Hemisphere compared to WACCM, up to 8°C in the Arctic. The 2°C difference observed in the Arctic is thus relatively small and in line with the bias already present in the models. The same is true for precipitation, with CAM having a bias towards wet tropics and a more southern ITCZ, with a positive difference of up to 1 mm/day.

The potential temperature response to the introduction of aerosols in the stratosphere compares exceptionally well, in magnitude and location in annual, JJA and DJF data. The most notable differences emerge in the polar regions in the middle to upper stratosphere, most likely attributed to the lack of ozone chemistry in CAM. Nevertheless, the large scale atmospheric circulation patterns respond in a highly similar fashion. CAM is able to reproduce the patterns from WACCM, that have also been observed previous studies (Bednarz et al. 2023b). The response is not uniform between the hemispheres though, especially the Polar Night Jet in the NH winter is markedly stronger in CAM compared to WACCM. With the exception of the high-latitude NH, the SAI emulator with CAM is able to reproduce the response of large scale atmospheric circulation to the deployment of SAI. We should also note that the data retrieved from CMIP6 for the Control simulation in WACCM only resolves three vertical layers between 30 and 3.5 hPa, less than half that of CAM, interfering with thorough analysis of this region.

The aim for Part I of this thesis was to verify if the emulator built with the simpler CAM could generally replicate the SAI experiment performed with the chemically comprehensive WACCM. We looked into global, regional and seasonal trends to identify where the two models diverge in their response to SAI. However, this is a study that considers only one run for each experiment. The conclusions based on this little data are tentative and more runs are necessary to definitively determine the success of the SAI emulator with CAM.

Part II

Southern Hemisphere Atmospheric Circulation

7 Methods Part II

7.1 Scenarios Used for the Simulations

All simulations considered in this second part were extended to 2130, where the forcing was kept constant at the 2100 levels. This extension provides further insight in the long-term effects of deploying SAI. Especially in the rapid cooling SAI scenario the extension provides time for the climate system to adjust to the ‘shock’ it experienced from SAI.

Shown in Figure 10 are the temperature targets from Equation 1 for the SSP5-8.5, gradual SAI and rapid cooling SAI simulations. After about 10 years of SAI the T_0 target is reached and maintained, like in the gradual SAI simulation. However, in contrast to the gradual SAI simulation, the rapid cooling SAI simulation is not able to return to and then maintain 2020 levels for T_1 and T_2 . In the rapid cooling SAI simulation both targets are overshot, though their levels are stabilised after 2100.

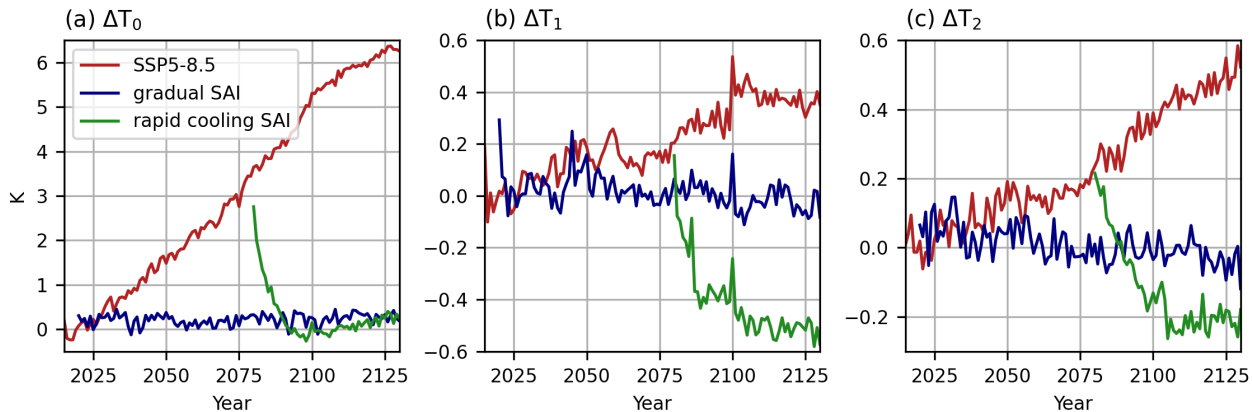


Figure 10: Deviations from temperature targets T_0 , T_1 , T_2 as compared to 2016-2025 mean, for Control, SAI 2020 and SAI 2080 scenarios in CAM.

7.2 Definition of Scenarios and Time Periods for Part II

Throughout this second part, four time periods are selected to visualise and interpret the results from the simulations. As in part I, for each period the 20-year mean is taken, unless specified otherwise. These periods are defined as follows:

- **Reference** The period 2016-2035 of the SSP5-8.5 simulation.
- **Control** The period 2111-2130 of the SSP5-8.5 simulation.

- **SAI 2020** The period 2111-2130 of the gradual SAI simulation.
- **SAI 2080** The period 2111-2130 of the rapid cooling SAI simulation.

7.3 Thermal Wind

The thermal wind is the vertical shear due to horizontal temperature variations. We can calculate the wind as the result of such temperature variations in the zonal and meridional direction through the thermal wind balance. With the vertical layers of the model converted to pressure coordinates, this equation takes the form

$$\frac{\partial v_g}{\partial p} = -\frac{R}{pf_0} \frac{\partial T}{\partial x}; \quad \frac{\partial u_g}{\partial p} = \frac{R}{pf_0} \frac{\partial T}{\partial y}, \quad (4)$$

where v_g, u_g is the geostrophic wind in meridional and zonal directions respectively, $R = 286.9 \text{ J kg}^{-1} \text{ K}^1$ is the specific gas constant for dry air, p is pressure, $f_0 = 2\Omega \sin \varphi$ is the coriolis parameter at the chosen reference latitude φ , $\frac{\partial T}{\partial x, y}$ is the layer-mean temperature gradient in zonal and meridional direction respectively. Rewriting and integrating gives us

$$\begin{aligned} \int_{p_0}^{p_1} \partial v_g &= \int_{p_0}^{p_1} -\frac{R}{f_0} \frac{\partial T}{\partial x} \partial \ln p; \\ \int_{p_0}^{p_1} \partial u_g &= \int_{p_0}^{p_1} \frac{R}{f_0} \frac{\partial T}{\partial y} \partial \ln p, \end{aligned} \quad (5)$$

where $p_{0,1}$ are the lower and upper boundaries of the model layer, respectively, so that $p_1 < p_0$. Because T is the layer-mean temperature and R and f_0 are constants, we can evaluate this integral to find the thermal wind in the layer between p_0 and p_1

$$\begin{aligned} v_T &= v_g(p_1) - v_g(p_0) = \frac{R}{f_0} \frac{\partial T}{\partial x} \ln \left(\frac{p_0}{p_1} \right); \\ u_T &= u_g(p_1) - u_g(p_0) = -\frac{R}{f_0} \frac{\partial T}{\partial y} \ln \left(\frac{p_0}{p_1} \right). \end{aligned} \quad (6)$$

To increase stability in our calculations, we assume that the thermal wind below 850 hPa is equal to the model wind, because the thermal wind calculation in the layers below that will most likely not produce stable results. To then find the integrated thermal wind at a given pressure coordinate above 850 hPa, we take the cumulative sum of the thermal wind from 850 hPa up to the given pressure plus the meridional or zonal wind of the layer below 850 hPa ($v(p_{<850}), u(p_{<850})$). This gives us for the integrated thermal wind at pressure coordinate p_t

$$\begin{aligned} v_T(p_i) &= v(p_{<850}) + \frac{R}{f_0} \sum_{i=0}^i \frac{\partial T_i}{\partial x} \ln \left(\frac{p_i}{p_{i+1}} \right), \\ u_T(p_i) &= u(p_{<850}) + \frac{R}{f_0} \sum_{i=0}^i -\frac{\partial T_i}{\partial y} \ln \left(\frac{p_i}{p_{i+1}} \right). \end{aligned} \quad (7)$$

7.4 Kinetic Energy and Eddy Kinetic Energy

The CAM model works with wind in the form of $u = \bar{u} + u^*$, $v = \bar{v} + v^*$, with u, v the total wind, \bar{u}, \bar{v} the monthly-mean wind and u^*, v^* the deviation from the mean wind. The model output contains monthly averages \bar{u}, \bar{v} and $\overline{u^2}, \overline{v^2}$.

The kinetic energy KE per unit mass can thus be found from the model results directly through

$$KE = \frac{1}{2} (\overline{u^2} + \overline{v^2}). \quad (8)$$

The eddy kinetic energy EKE per unit mass can be found through

$$EKE = \frac{1}{2} (\overline{u^{*2}} + \overline{v^{*2}}), \quad (9)$$

with $\overline{u^{*2}}, \overline{v^{*2}}$ found through

$$\begin{aligned} \overline{u^2} &= \overline{(\bar{u} + u^*)(\bar{u} + u^*)}, \\ &= \overline{\bar{u}^2} + 2\bar{u}u^* + \overline{u^{*2}}, \\ &= \overline{\bar{u}^2} + \overline{u^{*2}} \Rightarrow \overline{u^{*2}} = \overline{u^2} - \overline{\bar{u}^2}, \end{aligned} \quad (10)$$

which can be found with the model output.

To find the kinetic and eddy kinetic energy per unit volume, we multiply the results from Eq. 8 and 9 with the local density. Assuming an ideal gas, we approximate the density through

$$\rho = \frac{p}{RT}, \quad (11)$$

with p pressure, T temperature and R again the specific gas constant for dry air.

7.5 Jet Intensity Maps

To visualise the extent and intensity of an atmospheric jet, we introduce the jet intensity map. The map is made by counting the number of times the zonal wind or eddy kinetic energy surpasses a set threshold. Each timestep and coordinate is evaluated individually, after which the set is summed over time and the vertical dimension. This result is then normalised to the total the number of timesteps multiplied by the number of vertical model levels included in the analysis. This results in a fraction that represents the occurrence and vertical extent of the atmospheric jet. The threshold is chosen to be about 80% of the maximum of the zonal mean.

To visualise the Polar night jet (PNJ), in the upper stratosphere, and the subtropical jet (STJ), in the lower stratosphere, this method is applied to the zonal wind fields. For the eddy-driven jet (EDJ), also in the lower stratosphere, this method is applied to the eddy kinetic energy fields. For all jets the threshold and vertical selection are noted in the figure description.

7.6 Sudden Stratospheric Warmings in Monthly Mean Model Data

Typical metrics for SSWs rely on daily model data to identify an event. Metrics typically use the reversal of zonal-mean zonal wind at 10 hPa and 60°N/S, from westerly to easterly, the reversal of the meridional temperature gradient at 10 hPa above 60°N/S, changes in the geopotential height field or topology of the polar vortex, or a combination and/or variation of these. Additionally, metrics typically include temporal constraints, excluding events that occur within a certain number of days of another event, or events after which the atmosphere does not return to its winter state (final warming) before the end of the season (Butler et al. 2015).

Because we consider monthly mean data these metrics are inapplicable. We therefore use a modified approach. we consider the zonal-mean zonal wind at 10 hPa and 60°S and the area-weighted average temperature at 10 hPa above 60°S. We consider the atmosphere to be in an SSW-like state when the zonal wind decreases or the temperature increases significantly in the winter months.

8 Results Part II

8.1 Potential Temperature and Zonal Wind Anomaly

The zonal-mean potential temperature and potential temperature anomalies for Control, SAI 2020 and SAI 2080 are shown in Figure 11, for the annual, JJA and DJF mean. The black contours indicate the zonal-mean zonal wind in m/s.

In Control we see the potential temperature anomaly signature of increased greenhouse gases, warming at the surface and the troposphere, extending to the lower stratosphere and cooling in the upper stratosphere. The cooling trend in the upper stratosphere is present in SAI 2020 and SAI 2080 as well, but over the Antarctic SAI 2020 and SAI 2080 cool significantly more. With SAI the potential temperature increases where SAI is deployed in the lower stratosphere, concentrated between 15°S and 30°S around 50 hPa. The warming extends over the Antarctic only in the summer (DJF), because of the lack of incoming solar radiation during the polar night in winter (JJA). The stratosphere in SAI 2020 is about 2.5K warmer than in SAI 2080. The tropospheric temperatures are successfully held at present day values in either SAI scenario, within a margin of $\pm 2.5\text{K}$.

In JJA (winter) we see that the temperature anomaly in SAI 2020 and SAI 2080 is opposite of the trend in Control. The Antarctic stratosphere cools with SAI instead of warming as it does under global warming. In DJF (summer) the anomaly is much more comparable, with warming over the Antarctic in all scenarios.

The zonal winds are mostly driven by the meridional temperature gradient through the thermal wind balance. Qualitatively, we see in Reference that the subtropical jet (STJ) in the lower stratosphere forms above a steep meridional temperature gradient around 30°S.

We also see an increase in wind speed around 50°S where we would expect to see the eddy-driven jet (EDJ), also above a relatively steep meridional gradient. From the wind speeds alone it seems the EDJ is weaker than the STJ, however, we know that the EDJ is generally stronger. This is because of the waviness of the EDJ, so clear identification must follow from eddy-activity, covered in Section 8.2.2.

Because the STJ and EDJ and their anomalies are strongest in winter, we will focus on this season in any further analysis of these jets in the lower stratosphere.

In the upper stratosphere we see in JJA a strong westerly wind, the polar night jet (PNJ). Comparison of the winter and summer meridional temperature gradient reveals that this jet is driven by temperature gradients as well. The meridional temperature gradient is positive (equator-to-pole) in JJA, resulting in strong westerlies. In DJF the gradient flattens in the stratosphere – even turning slightly negative in the upper stratosphere - preventing strong westerly winds from forming.

In all scenarios the PNJ shifts equatorward, in Control because the latitude of the highest temperature gradient shifts over the whole stratosphere, in SAI 2020 and SAI 2080 because the temperature gradient strongly increases on the equatorward side in the lower stratosphere. This will be discussed in more detail in Section 8.3.

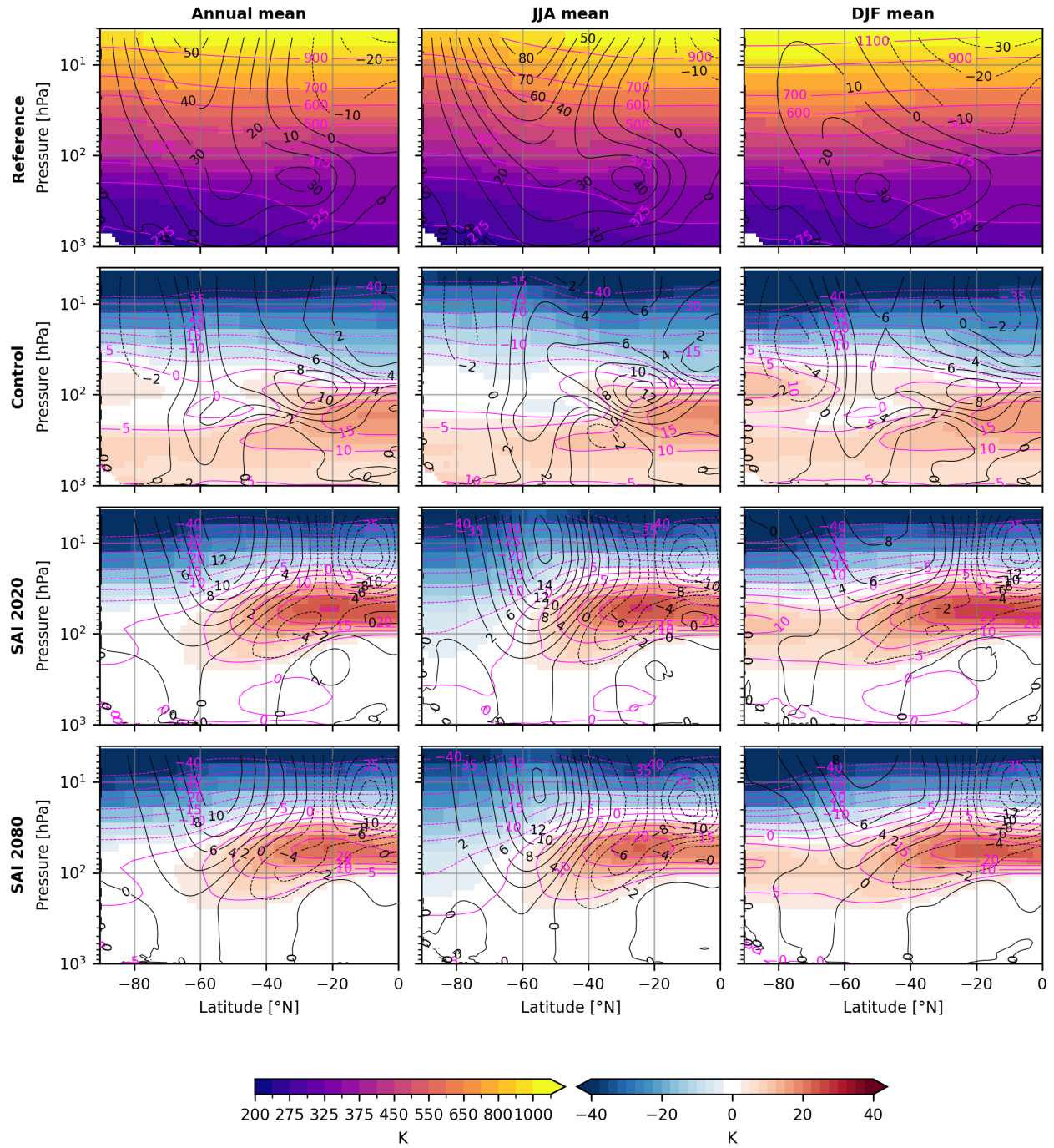


Figure 11: Annual and seasonal mean zonal-mean potential temperature (shading and magenta contours) and zonal-mean zonal wind (black contours, m/s) for Reference (first row) and Control, SAI 2020 and SAI 2080 anomaly compared to Reference (second to fourth row).

8.2 Results Part II: Lower Stratosphere

8.2.1 Subtropical Jet

In Figure 11 the zonal mean of the zonal component of the integrated thermal wind is shown, together with the observed zonal-mean zonal wind in black contours. The observed wind and integrated thermal wind show a strikingly similar pattern, with the observed wind consistently lower than the integrated thermal wind due to friction effects, increasingly so further up in the atmosphere.

The change in magnitude of the lower stratosphere wind strongly correlates with the change in magnitude of the integrated thermal wind. The STJ shifts upward and equatorward in Control, also showing a significant increase of up to 12 m/s in the upper regions. This pattern is consistent with the change in potential temperature in Figure 11. See also Figure 26 in Appendix B, the meridional gradient of the 350K isotherm is much steeper around 30°S in Control compared to Reference.

In contrast, in both SAI 2020 and SAI 2080 the STJ decreases in strength, up to 6 m/s in the upper regions around 100 hPa. This possibly also indicates an equatorward shift, but slightly downward instead of upward.

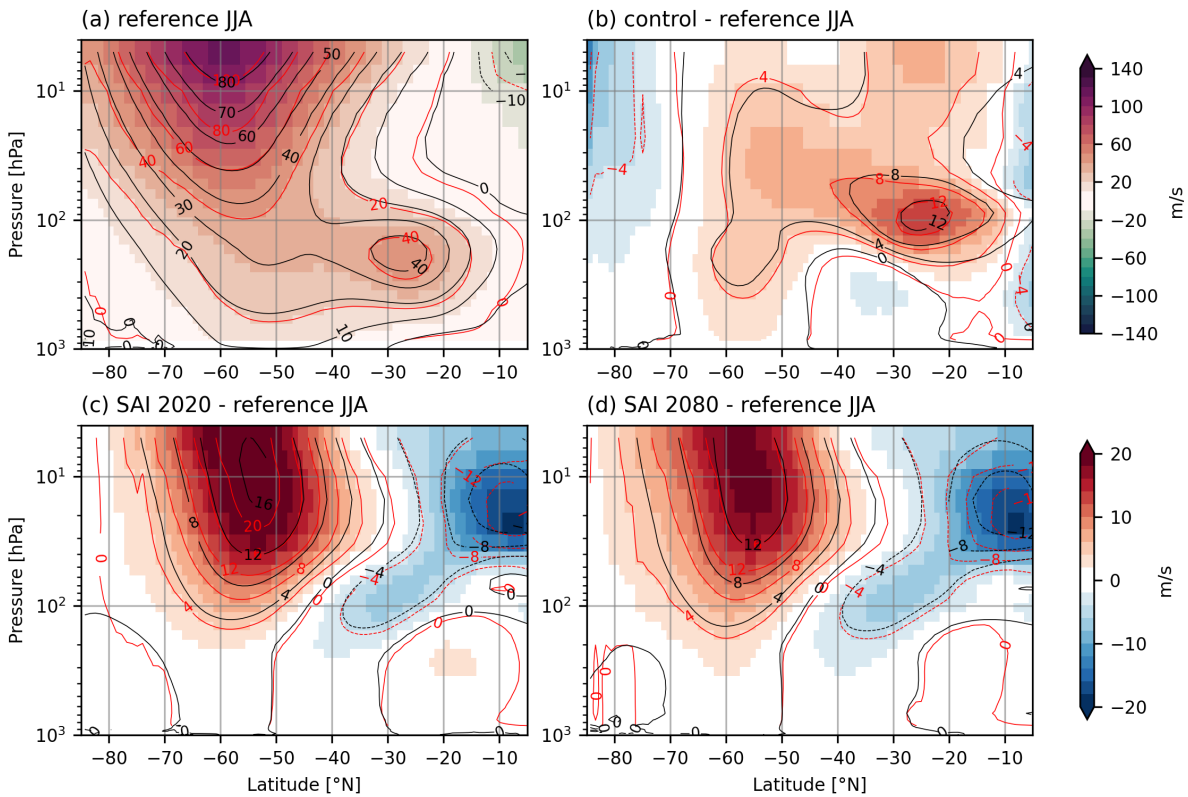


Figure 12: JJA mean zonal-mean zonal thermal wind (shading and red contours) and zonal-mean zonal wind (black contours, m/s) for (a): Reference; (b-d): Control, SAI 2020 and SAI 2080 anomaly compared to Reference.

On the subtropical jet intensity map in Figure 13 the same trends as above are observed. In Control the jet intensifies and shifts equatorward. The largest increase is observed in the eastern

Pacific Ocean, in Reference the jet is relatively weak in this region, but in Control the jet is the at its peak here. The area between 120°W and 60°E increases the most relatively, the opposite hemisphere shows little change.

In SAI 2020 and SAI 2080 the jet is much less intense, but the spatial distribution remains largely unchanged. The jet weakens slightly more in SAI 2080 than in SAI 2020, but the difference does not seem significant.

The location, height and mean of the maximum of the STJ reported in Figure 14 largely confirm the patterns observed above. In Control, the STJ maximum shifts equatorward between 120°W and 60°E and remains around the position of Reference in the other hemisphere, correlating to the increase in intensity. The upward shift of the maximum is about 25 hPa, and the mean maximum wind speed increases 6.2 m/s, or 12.7%.

The maximum wind speed in SAI 2020 and SAI 2080 remains mostly at Reference levels, deviating at most 1.1 m/s, or 2%, in SAI 2020 which is not significant. As the maximum wind speed does not change considerably, but the jet does appear much less intense, this means the jet has become more constrained without losing much strength at its maximum. The location of the maximum in SAI 2020 and SAI 2080 has not shifted much overall, only significantly around 60°E . Looking at the intensity in Figure 13 this seems to be the result of the wind speeds in the eddy-driven jet (around 50°S) reaching similar levels as the STJ jet. The EDJ effectively competes with the STJ for the maximum wind speed and ‘wins’ a considerable amount of times.

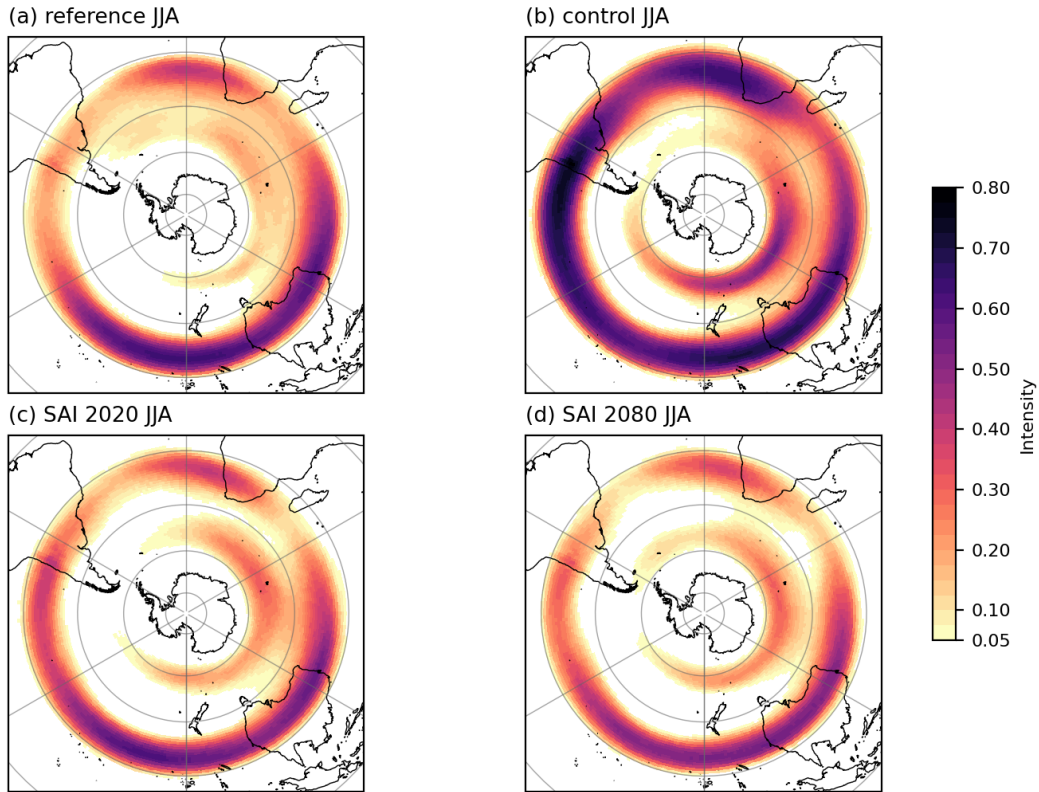


Figure 13: JJA subtropical jet intensity map of zonal wind, values counted when the threshold of 40 m/s was passed between 400 and 100 hPa, for (a) Reference, (b) Control, (c) SAI 2020 and (d) SAI 2080. 0°E is oriented towards the top of the figure.

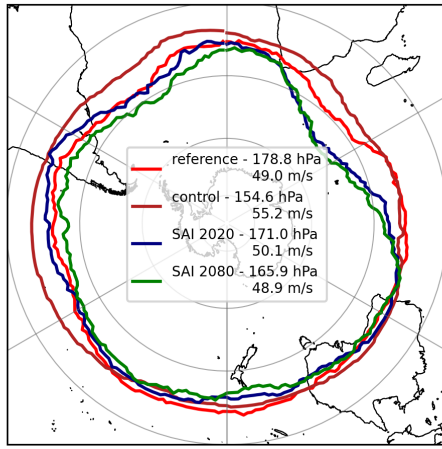


Figure 14: JJA mean location of the maximum of the subtropical jet, with corresponding longitudinal mean height and maximum eddy kinetic energy for Reference, Control, SAI 2020 and SAI 2080. 0°E is oriented towards the top of the figure.

8.2.2 Eddy-driven Jet

The EDJ is already visible in Figure 13. The zonal wind in the Eastern Hemisphere reveals another jet structure next to the STJ. Because this jet is driven by eddy activity, the zonal wind alone will not reveal much on its behaviour. We use eddy kinetic energy (EKE) as a measure for eddy activity. The zonal-mean EKE and EKE anomalies are shown in Figure 15.

Around 50°S and 300 hPa, there is a peak in EKE, i.e. high eddy activity, this is where we identify the EDJ to be. In Control the EKE decreases on the lower equatorward side of the jet and increases on the upper poleward side, indicating that the jet shifts poleward and upward. It is not clear from this figure if the jet becomes more or less wavy. In SAI 2020 and SAI 2080 the EKE shows small changes compared to what is observed in Control. A slight decrease is observed around 45°S, in the area between the EDJ and the STJ, and stays close to Reference levels everywhere else. SAI 2020 responds more strongly than SAI 2080.

The eddy-driven jet intensity map in Figure 16 also indicates an increase in intensity in Control and a poleward shift. The change in intensity in SAI 2020 and SAI 2080 is again much smaller, both weakening slightly while the overall spatial pattern remains largely unchanged.

The location of the maximum in Figure 17 reveals that the EDJ remains largely in position in both SAI scenarios, but shifts poleward everywhere in Control. The upward shift identified in Figure 15 in Control is confirmed to be about 23 hPa. In SAI 2020 and SAI 2080 the jet maximum shifts slightly downward, though not significantly. In each scenario the mean maximum EKE decreases slightly but insignificantly, 2-4%, again not providing much insight into any changes waviness of the jet.

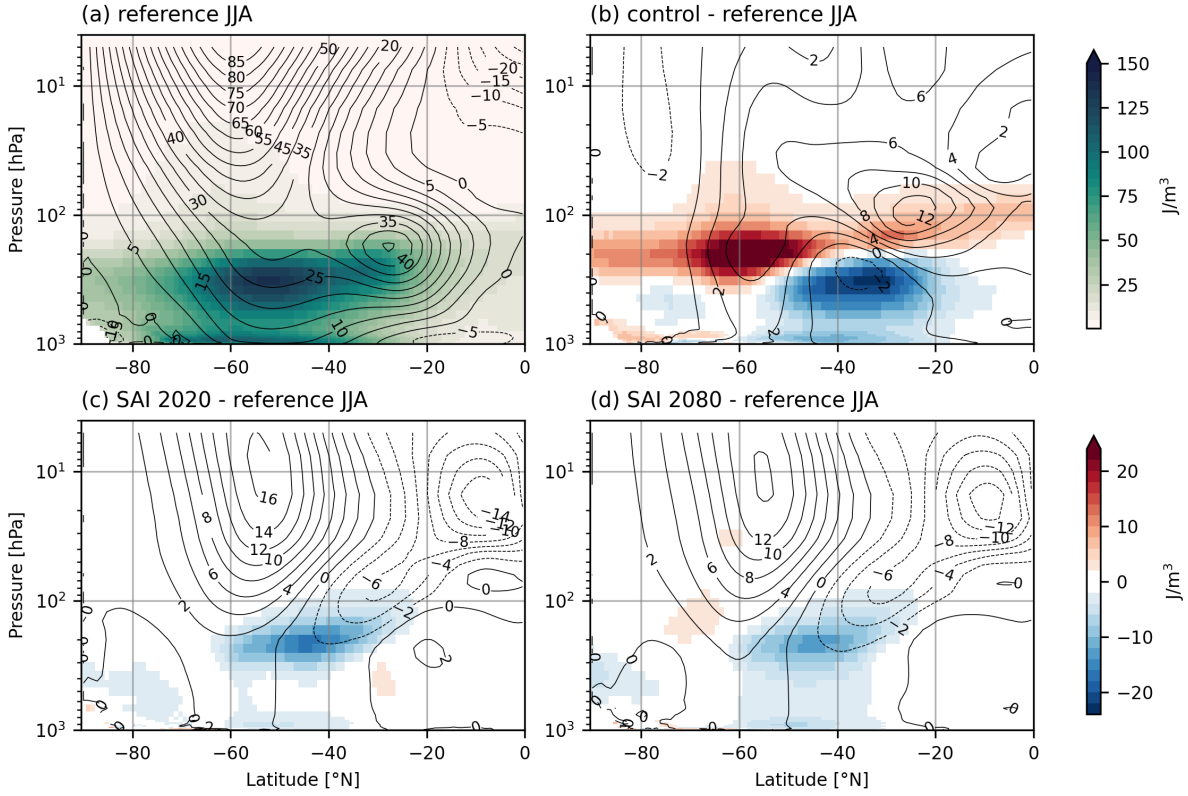


Figure 15: JJA mean zonal-mean eddy kinetic energy (shading) and zonal-mean zonal wind (contours, m/s) for (a): Reference; (b-d): Control, SAI 2020 and SAI 2080 anomaly compared to Reference.

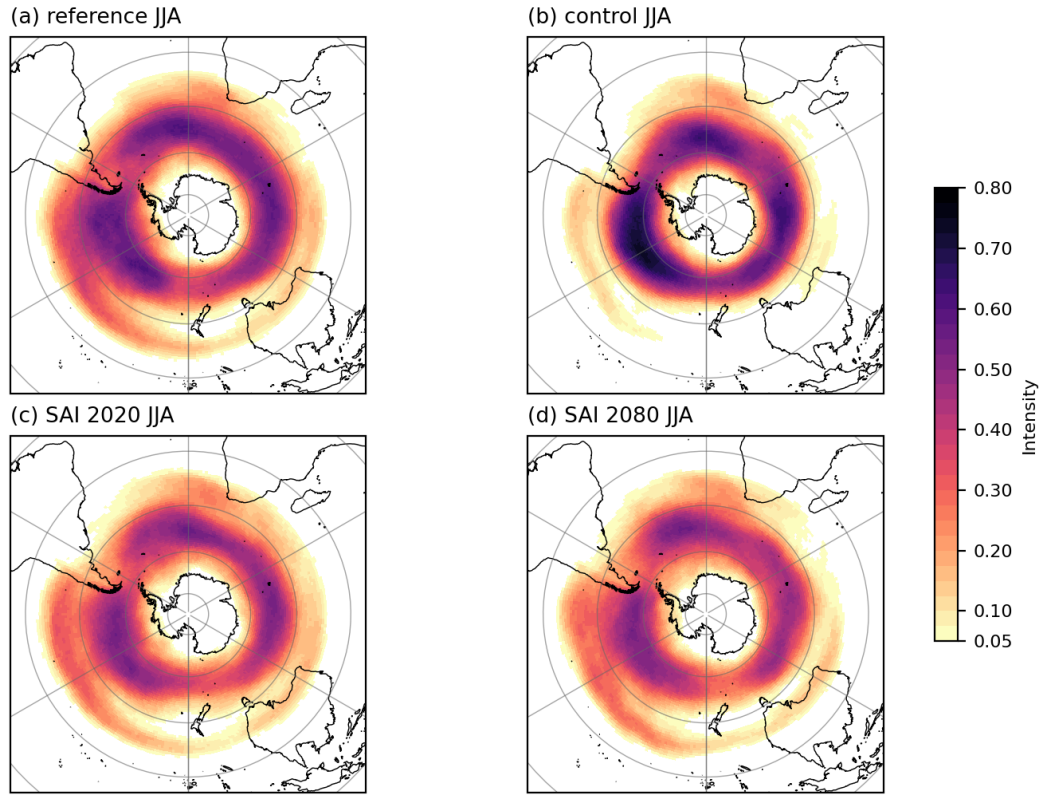


Figure 16: JJA eddy-driven jet intensity map of EKE, values counted when the threshold of 105 J/m^3 was passed between 600 and 150 hPa, for (a) Reference, (b) Control, (c) SAI 2020 and (d) SAI 2080. 0°E is oriented towards the top of the figure.

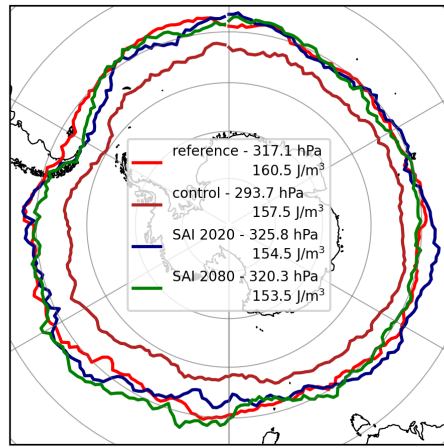


Figure 17: JJA mean location of the maximum of the eddy-driven jet, with corresponding longitudinal mean height and maximum eddy kinetic energy for Reference, Control, SAI 2020 and SAI 2080. 0°E is oriented towards the top of the figure.

The STJ has more kinetic energy than the EDJ, mostly because of the higher mean wind speeds. The EDJ has a proportionally larger eddy component and thus higher EKE. Comparing the changes in KE and EKE and zonal wind speed will provide insight into the waviness of the two jets.

In Figure 18 the zonal-mean kinetic energy and zonal-mean zonal wind are shown. In Control the increase in KE follows the zonal wind patterns in sign and in magnitude. The KE increases with the increasing zonal wind accordingly in the upper regions of the STJ and decreases proportionally below. The KE also increases proportionally to wind speed in the EDJ. This indicates that the STJ and the EDJ do not become significantly more or less wavy under global warming.

For SAI 2020 and SAI 2080 the KE anomaly follows the zonal wind anomaly proportionally as well. Comparison with Figure 15 shows that the decrease in EKE for the EDJ is correlated with the decrease in zonal wind. The decrease in KE in the STJ shows that the constraining of the jet observed in Figure 13 leads to a loss of strength, even while maintaining maximum wind speed.

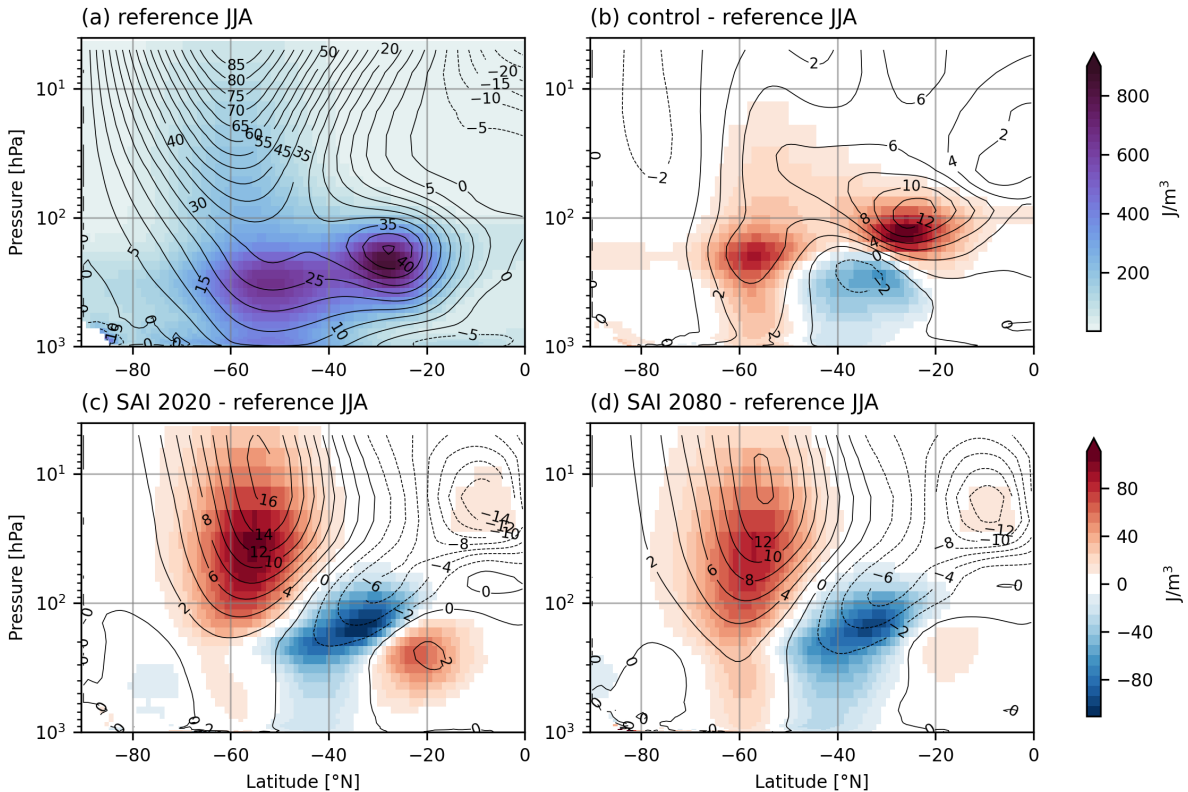


Figure 18: JJA mean zonal-mean kinetic energy (shading) and zonal-mean zonal wind (contours, m/s) for (a): Reference; (b-d): Control, SAI 2020 and SAI 2080 anomalies compared to Reference.

8.3 Results Part II: Upper Stratosphere

Because the polar night jet is strongest in the late winter to early spring, we will consider the August-September-October (ASO) mean in our analysis of the PNJ. Sudden stratospheric warming events will also be discussed in this section.

8.3.1 Polar Night Jet

As was discussed above, in all scenarios the PNJ shifts equatorward, in Control because the latitude of the highest temperature gradient shifts, in SAI 2020 and SAI 2080 because the temperature gradient in the lower stratosphere strongly increases. Figure 19 shows the zonal component of the integrated thermal wind and the anomalies in Control, SAI 2020 and SAI 2080 in ASO. As in section 8.2, the observed wind and the integrated thermal wind show the same patterns, with the integrated thermal wind consistently higher than the observed wind due to friction effects.

In Figure 19 we see that the PNJ indeed shifts equatorward in Control, confirming that the changes in the PNJ are governed by thermal changes under global warming. Its strength does not significantly change either way. In SAI 2020 and SAI 2080 the PNJ shifts equatorward as well, also governed by thermal changes from SAI, but in contrast to Control the wind speed increases significantly. The pattern in SAI 2080 is the same as in SAI 2020, but the increase is at least 4 m/s less.

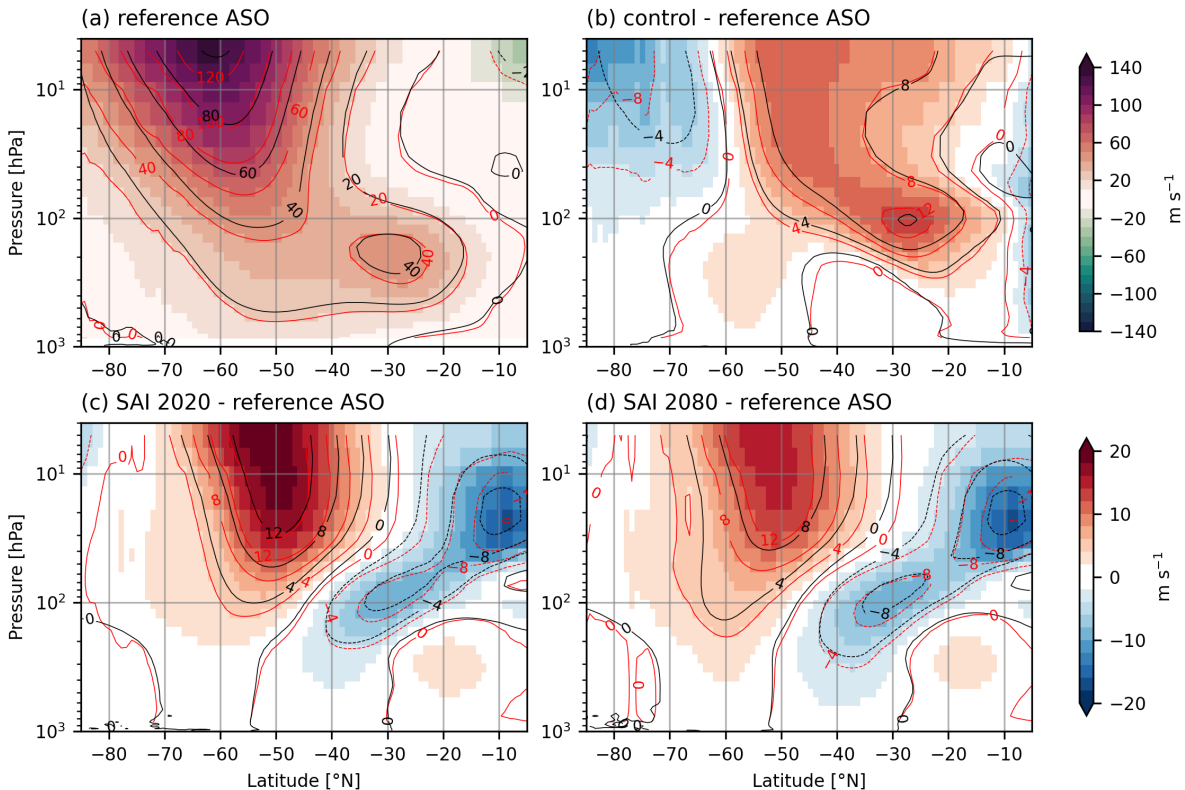


Figure 19: ASO mean zonal-mean integrated thermal wind (shading and red contours) and zonal wind (contours, m/s) for (a): Reference; (b-d): Control, SAI 2020 and SAI 2080 anomaly compared to Reference.

The changes in kinetic energy per unit mass shown in Figure 20 correspond well with the changes in integrated thermal wind in Figure 19. The eddy kinetic energy in Figure 21 shows a different picture. In Control there is a stark decrease in EKE on the poleward side of the PNJ. This decrease is very large relative to the KE decrease, indicating a deacrease in eddy activity.

The decrease in EKE over the Antarctic is visible in SAI 2020 and SAI 2080 as well, though not as intensely. It still indicates a decrease in eddy activity. In the interior of the PNJ, where the KE increase is largest, the EKE shows a more broad increase. Most strikingly, in both SAI scenarios the EKE increases a little bit less where the zonal wind is strongest. Instead, the EKE increases the most on the flanks of the jet, indicating the jet becomes more broad and wavy. The magnitude by which this happens seems to correspond to the wind speed, as again SAI 2080 is slightly weaker than SAI 2020.

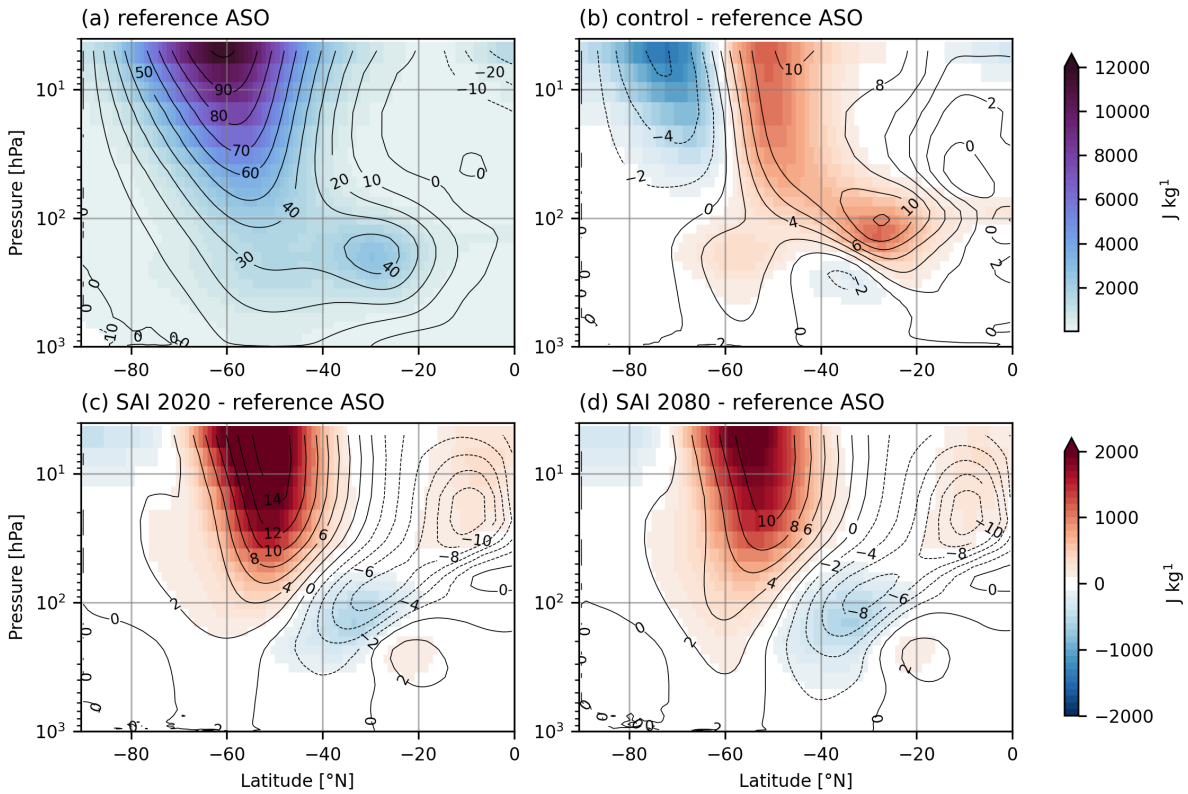


Figure 20: JJA mean zonal-mean kinetic energy (shading) and zonal wind (contours, m/s) for (a): Reference; (b-d): Control, SAI 2020 and SAI 2080 anomaly compared to Reference.

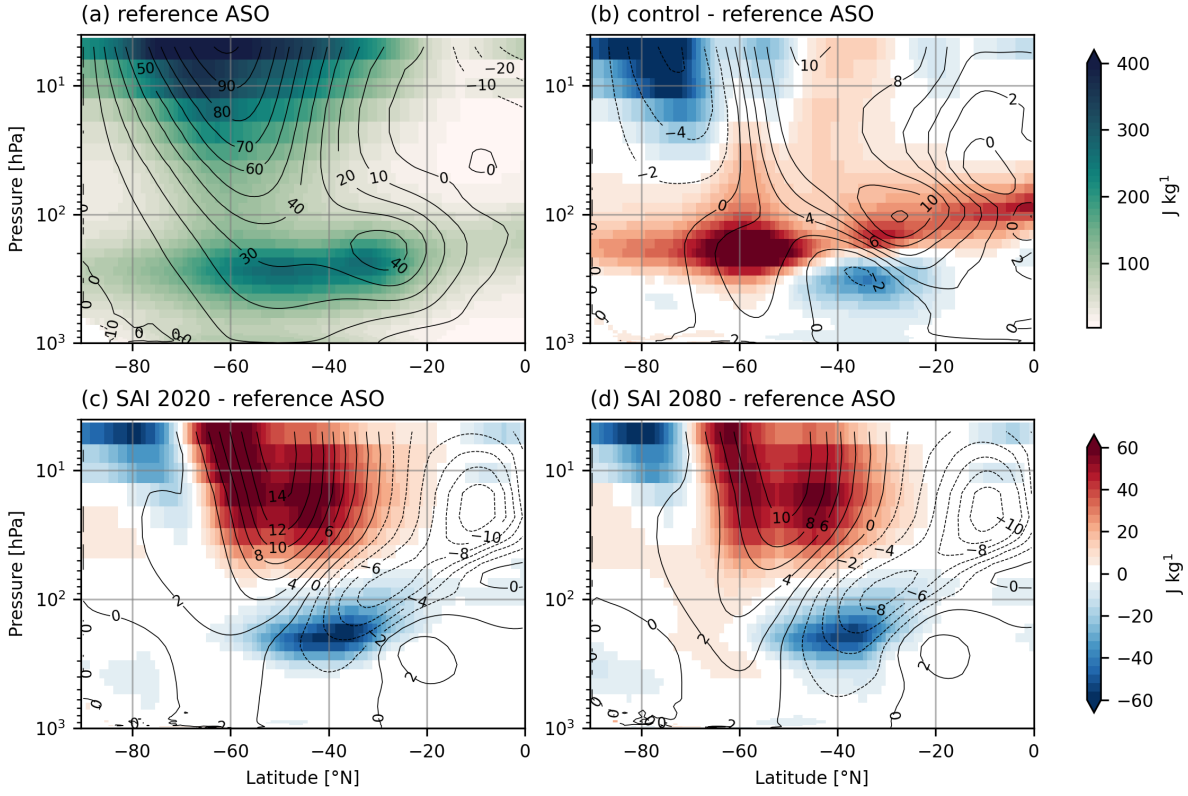


Figure 21: JJA mean zonal-mean eddy kinetic energy (shading) and zonal wind (contours, m/s) for (a): Reference; (b-d): Control, SAI 2020 and SAI 2080 anomalies compared to Reference.

The intensity map of the PNJ is shown in Figure 22. The PNJ intensifies in all scenarios, most strongly in SAI 2020, followed by SAI 2080 and lastly Control. This increase in control was not apparent from the zonal mean figures, possibly because the increase is not zonally uniform. The PNJ indeed grows more broad in SAI 2020 and SAI 2080, as observed above. The equatorward shift in all scenarios is more clearly observed in Figure 23, where the mean location of the maximum observed wind speed is shown. The scenario with the largest shift varies per location, with hardly any shift in any scenario in the 0° - 60° E section, Control shifting the most in the 120° - 180° E section, and SAI 2020 shifting the most in the 240° - 300° E section. The shift in SAI 2080 is mostly consistent with SAI 2020, but deviates in the 240° - 300° E section, coinciding with Control there instead. Maximum wind speed remains at Reference levels in Control, but increases by 8.0 m/s, or 8.3%, in SAI 2020 and 6.2 m/s, or 6.4%, in SAI 2080.

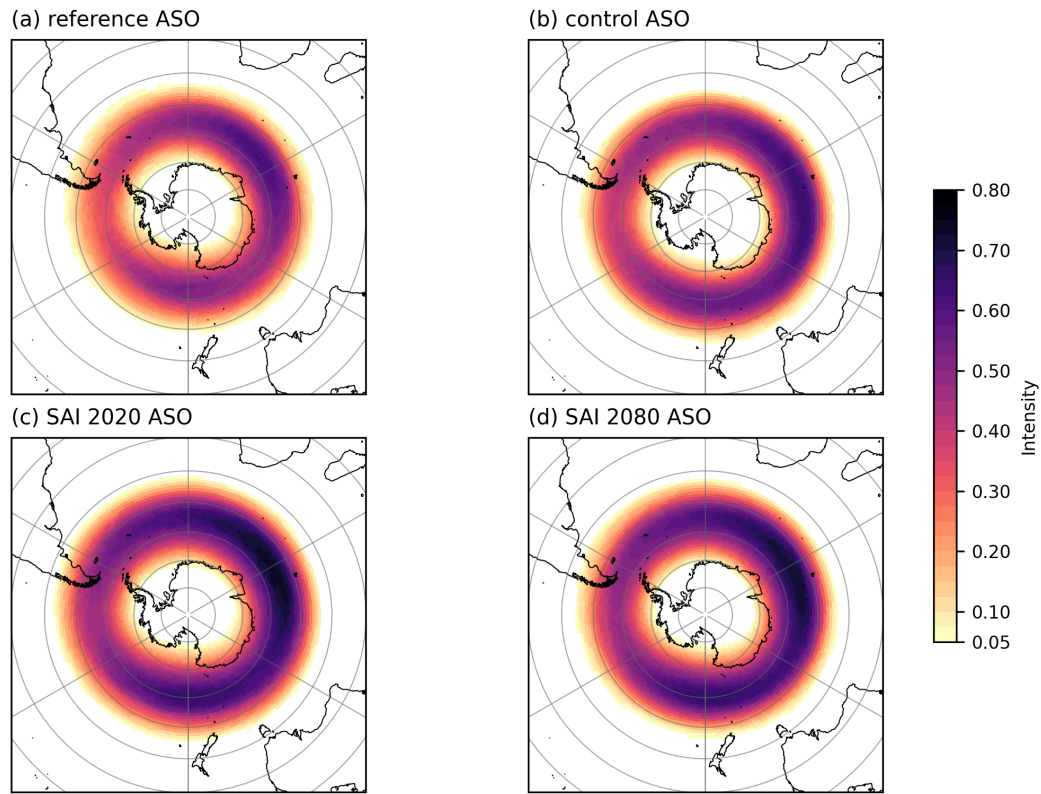


Figure 22: Polar night jet intensity map of zonal wind, values counted when the threshold of 80 m/s was passed at 10 hPa, for (a) Reference, (b) Control, (c) SAI 2020 and (d) SAI 2080. 0°E is oriented towards the top of the figure.

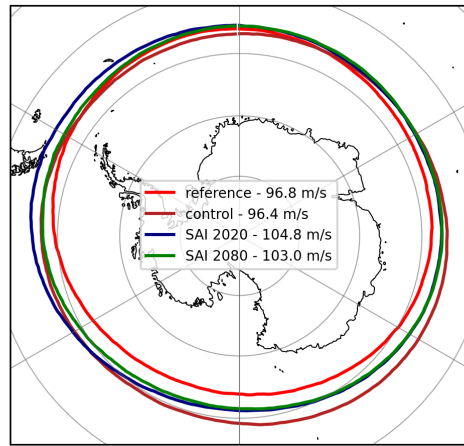


Figure 23: Mean location of maximum wind speed at 10 hPa, with longitudinal mean maximum wind speed, for Reference, Control, SAI 2020 and SAI 2080. 0°E is oriented towards the top of the figure.

8.3.2 Sudden Stratospheric Warming Events

The decrease in EKE over the Antarctic observed in 21 suggests a decrease in the occurrence of sudden stratospheric warming events (SSW). Figure 24 shows the area weighted mean temperature of the 10 hPa level above 60°S, together with the zonal wind at 10 hPa and 60°S. In Reference there is a number of years where the temperature increases, and a number of years the zonal wind decreases compared to the mean. Though not explicitly identified, this happens in pairs, when the temperature rises, the winds decrease. In Control the frequency of these SSW-like conditions decreases significantly, the temperature and zonal wind bands narrow compared to Reference. In SAI 2020 there appears to be one year with SSW-like conditions, but again the temperature and zonal wind bands narrow. SAI 2080 shows the same trend.

In all scenarios the zonal wind increases, as was already discussed in the results above, and the temperature decrease due to increased greenhouse gases is also visible. In all scenarios the PNJ forms earlier in the year, surpassing 80 m/s in early to mid-July in Control and in mid-June in SAI 2020 and SAI 2080, as opposed to mid-July in Reference. The PNJ also dissolves later in the year, decreasing to 80 m/s in late October in Control and early November in SAI 2020 and SAI 2080, as opposed to mid-October in Reference.

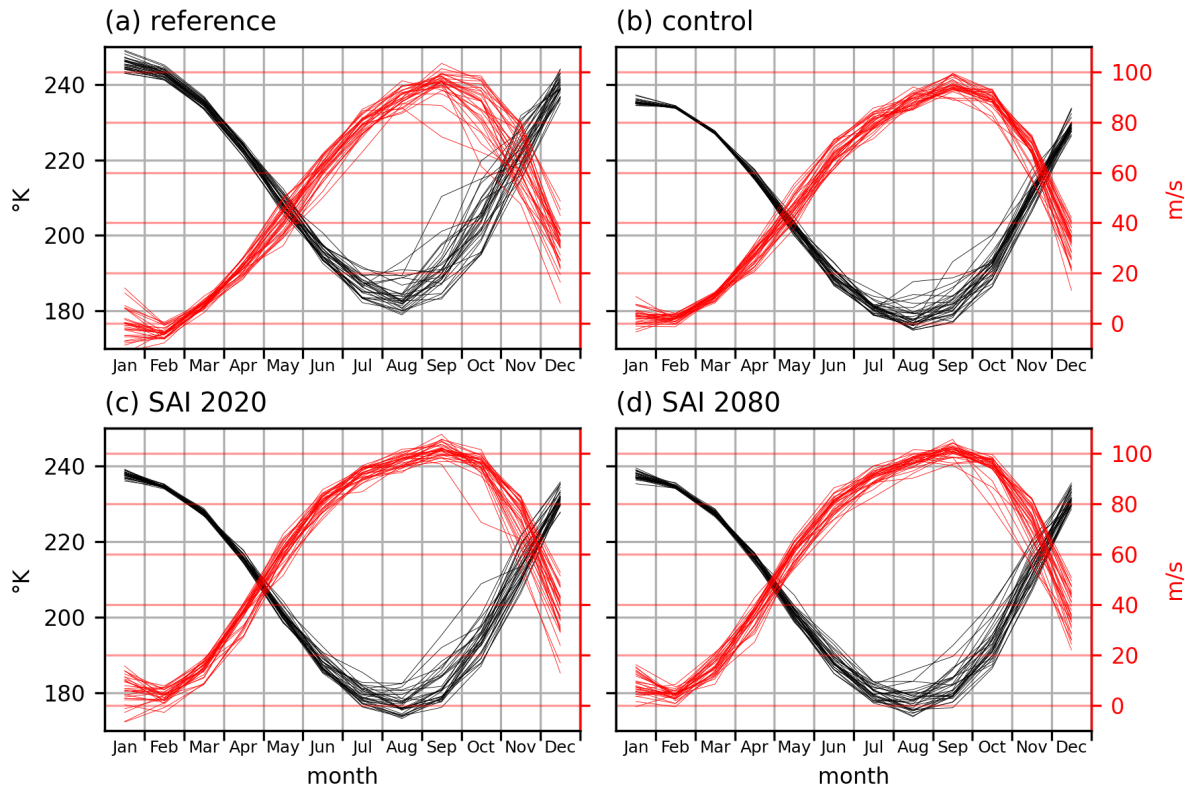


Figure 24: Climograph of area-weighted mean temperature of 60°-90°S at 10 hPa (black) and zonal-mean zonal wind at 60°S and 10 hPa (red) for (a) 2016-2045 and (b) 2101-2130 in the SSP5-8.5 experiment, (c) 2101-2130 in the gradual SAI experiment and (d) 2101-2130 in the rapid cooling SAI experiment.

9 Discussion Part II

In our experiments of SAI the introduction of aerosols causes the signature stratospheric warming observed in previous studies (Ammann et al. 2010; Bednarz et al. 2023b). Atmospheric dynamical changes are predominantly governed by this thermal response, as they are in present day climate.

We observe the subtropical jet to shift equatorward and increase strongly under global warming, which is directly opposite of the equatorward and decreasing trend observed in previous studies (Chenoli et al. 2017). We also do not observe that the jet becomes wavier as was found by Martin and Norton (2023). It is not clear why our model exhibits this behaviour, but the dynamical change is consistent with the model's thermal response. We will thus treat this as the trend to be prevented by SAI.

Within our model SAI prevents the changes in the STJ very well. Because the temperatures in the troposphere are kept generally at Reference levels, we do not observe large changes in the STJ. Most change appears to be contained within the upper regions of the jet where the stratosphere has warmed considerably, leading to a slight decrease in overall intensity and kinetic energy within the jet.

The eddy-driven jet is situated in an area that experiences little to no thermal changes under SAI. The stark poleward shift and increase in strength we observe under high global warming, also observed in previous studies (Curtis et al. 2020), is prevented very well by SAI. As zonal wind speeds increase slightly and eddy activity decreases slightly (mainly on the equatorward side), we conclude that the EDJ becomes slightly less wavy under SAI. In this sense, SAI slightly overshoots its correction of the effects of high global warming.

The most significant effect of SAI occurs in the upper stratosphere in the polar night jet, above the stratospheric warming. This change is undeniably caused by this thermal response as is clear from the integrated thermal wind. The PNJ shifts equatorward and becomes generally more broad, more wavy. This equatorward shift is of the same magnitude as observed under high global warming, but geographically distinct. It is not entirely clear if the effect of greenhouse gases have a compounding effect on the PNJ shift, but it is unlikely because of the regionally differing response.

The PNJ has been shown to influence the EDJ, which could explain the changes in the EDJ. However, in the Southern Hemisphere this connection is strongest in late spring and summer (Ceppi and Shepherd 2019). Notably the delayed breakdown of the PNJ favours a poleward shift of the EDJ. It is possible this effect is visible in Figure 28 in Appendix D, but the location of the maximum EKE in Figure 29 does not support this.

In all scenarios the frequency of sudden stratospheric warming events appears to decrease. The atmosphere is less frequently in an SSW-like state, the yearly variability in 10 hPa temperature and zonal wind decreases significantly. This is expected under high global warming (Jucker et al. 2021), and SAI is not able to completely prevent this. It should be noted that one 30-year span for each scenario is not enough to confidently assess observed changes in the frequency of major SSWs. In the SH these events occur once every 22 years, thus a sample containing 30 years is not enough to determine a change in frequency. Additionally, this analysis only identifies if the atmosphere appears to be in a SSW-like state. For true assessment of SSWs, both major and minor events, daily model output is required.

Because we use only one run for each scenario, interpretation of these results remains limited. Our results do align with previous research, so this method of using an emulator is worth pursuing for the study of atmospheric dynamics in the context of SAI.

The general difference between the gradual SAI and the rapid cooling SAI experiments is that the gradual SAI experiment has a slightly weaker response. It is not entirely clear why this response is weaker, whether the prolonged warming of the earth system has direct effects or if the slightly different aerosol burden is to blame. The 2-meter temperature in SAI 2080 in Figure 27(d) shows a comparable response to SAI 2020. The warming hole is considerably larger in SAI 2080, as described in Pflüger et al. (2024) due to increased weakening of the atlantic meridional overturning circulation, which might explain the slight warming observed in the SH as well. It is also possible that the aerosol response is weaker because the warming hole creates a cool bias, leading to warming over the remainder of the globe. Nevertheless, the SAI 2080 is still an objectively good SAI scenario, able to prevent the effects of global warming, especially increasing surface temperature.

10 Conclusions and Outlook

10.1 Part I: Model Validation

When applying the stratospheric aerosol emulator to a gradual SAI scenario in CESM2(CAM6), are we able to reproduce from Tilmes et al. (2020)

i the temperature targets T_0 , T_1 and T_2 ?

The temperature targets are reached with similar end results and similar variability. Though the CAM response to the SSP5-8.5 scenario is significantly different from WACCM, the emulator with CAM is able to maintain 2020 levels for each target as well as WACCM is able to.

ii the spatial and seasonal variations of temperature, precipitation and general aspects of the atmospheric circulation?

The surface temperature pattern observed in CAM varies from WACCM regionally, but globally corresponds well to WACCM. The differences in temperature are well within the range of inter-model variability. The precipitation patterns in CAM and WACCM agree overall, but the inter-model differences are larger than for the surface temperature. The difference in precipitation change mostly reflects model bias, with CAM favouring wetter tropics and a stronger southward shift of the ITCZ.

The stratospheric warming from the injection of aerosols is nearly identical. The lack of ozone chemistry in CAM does appear to cause some additional cooling in the middle to upper stratosphere over the poles, but this does not cause concerning differences in the dynamical response of the model. The atmospheric dynamics of WACCM are replicated well by CAM, especially in the Southern Hemisphere.

10.2 Part II: Southern Hemisphere Atmospheric Circulation

What are the impacts of the gradual SAI scenario on the Southern Hemisphere

i subtropical and eddy-driven jets in the lower stratosphere?

The changes in the subtropical observed under the SSP5-8.5 scenario are prevented by SAI very well. The general and maximum wind speed are conserved, but the upper regions experience a small decrease, leading to an overall slight decrease in jet intensity and kinetic energy. The strong poleward shift of the EDJ is prevented almost completely by SAI. The EDJ does appear to become slightly less wavy, mostly on the equatorward side of the jet. The overshoot of SAI in both jets is small compared to the magnitude of change under global warming.

ii polar night jet and sudden stratospheric warming events in the upper stratosphere?

The polar night jet is most affected by SAI compared to the STJ and the EDJ. The thermal response of the stratosphere leads to a strong equatorward shift and a considerable increase in strength. The equatorward and increasing trend observed under the SSP5-8.5 scenario is surpassed under SAI, with the jet growing more intense, broad and wavy. The PNJ grows more stable under SAI than present day climate and the frequency of sudden stratospheric

warming events decreases significantly. Though the stability of the PNJ does not increase as much under SAI, SAI is not able to prevent this downward trend from emerging.

How do the results for i and ii change under the rapid cooling SAI scenario? For all trends observed in the atmospheric dynamics, the response from SAI 2080 is slightly weaker. This could be a result of the prolonged warming preceding the employment of SAI or slight differences in the exact employment of SAI due to the prolonged warming. The changes are very small and do not undermine the assertion that the rapid cooling scenario is objectively successful and does not lead to vastly different behaviour in the atmospheric circulation in the Southern Hemisphere.

10.3 Outlook

The emulator studied in this thesis is promising as a tool to explore the climate response to SAI scenarios while using comparatively limited computing resources. As with any climate model, a higher resolution experiment would provide better insight into precipitation changes. Higher resolution experiments also allow for analysis of sub-mesoscale phenomena like tropical cyclones. Analysis of daily model output would allow for a better assessment of sudden stratospheric warming events. Daily data also provides opportunities to study surface processes and weather, and possible teleconnections with the stratosphere. If computational resources allow it, expanding the temperature goals included in the feedback algorithm in the emulator could improve its performance. Adding a meridional component to the adjustment of the aerosol field could possibly open the door to more complex SAI scenarios that stray further from the SAI scenario the emulator was based on.

Acknowledgements

First of all I would like to thank my supervisors Claudia Wieners, Michiel Baatsen and Jasper de Jong for their guidance, wisdom and understanding, and the weekly meetings that were as fun as they were productive. In particular Claudia for sharing her expertise on geoengineering and guiding me through the process of doing research, Michiel for sharing his seemingly endless knowledge on the atmosphere, and Jasper for helping me with the numerous technical and practical issues I encountered along the way.

I would also like to thank Daniel Pflüger for the use of his dataset and helping me get started with my analysis of it, and for the comradery among activists at IMAU.

I want to thank Willem for his support and care, helping me get through these past months. And lastly thanks to my friends and family for their support and encouragement and my fellow students for the warm atmosphere in the IMAU Master's room.

References

- Ammann, Caspar M., Warren M. Washington, Gerald A. Meehl, Lawrence Buja, and Haiyan Teng (2010). “Climate engineering through artificial enhancement of natural forcings: Magnitudes and implied consequences”. In: *Journal of Geophysical Research: Atmospheres* 115.D22. doi: <https://doi.org/10.1029/2009JD012878>.
- Bednarz, E. M., A. H. Butler, D. Visioni, Y. Zhang, B. Kravitz, and D. G. MacMartin (2023a). “Injection strategy – a driver of atmospheric circulation and ozone response to stratospheric aerosol geoengineering”. In: *Atmospheric Chemistry and Physics* 23.21, pp. 13665–13684. doi: [10.5194/acp-23-13665-2023](https://doi.org/10.5194/acp-23-13665-2023).
- Bednarz, E. M., D. Visioni, B. Kravitz, A. Jones, J. M. Haywood, J. Richter, D. G. MacMartin, and P. Braesicke (2023b). “Climate response to off-equatorial stratospheric sulfur injections in three Earth system models – Part 2: Stratospheric and free-tropospheric response”. In: *Atmospheric Chemistry and Physics* 23.1, pp. 687–709. doi: [10.5194/acp-23-687-2023](https://doi.org/10.5194/acp-23-687-2023).
- Bednarz, Ewa M., Daniele Visioni, Amy H. Butler, Ben Kravitz, Douglas G. MacMartin, and Simone Tilmes (2023c). “Potential Non-Linearities in the High Latitude Circulation and Ozone Response to Stratospheric Aerosol Injection”. In: *Geophysical Research Letters* 50.22. e2023GL104726 2023GL104726, e2023GL104726. doi: <https://doi.org/10.1029/2023GL104726>.
- Butler, Amy H., Dian J. Seidel, Steven C. Hardiman, Neal Butchart, Thomas Birner, and Aaron Match (2015). “Defining Sudden Stratospheric Warmings”. In: *Bulletin of the American Meteorological Society* 96.11, pp. 1913–1928. doi: [10.1175/BAMS-D-13-00173.1](https://doi.org/10.1175/BAMS-D-13-00173.1).
- Ceppi, Paulo and Theodore G. Shepherd (2019). “The Role of the Stratospheric Polar Vortex for the Austral Jet Response to Greenhouse Gas Forcing”. In: *Geophysical Research Letters* 46.12, pp. 6972–6979. doi: <https://doi.org/10.1029/2019GL082883>.
- Chenoli, Sheeba Nettukandy, Muhammad Yunus Ahmad Mazuki, John Turner, and Azizan Abu Samah (2017). “Historical and projected changes in the Southern Hemisphere Sub-tropical Jet during winter from the CMIP5 models”. In: *Climate Dynamics* 48, pp. 661–681. doi: <https://doi.org/10.1007/s00382-016-3102-y>.
- Curtis, Paul Edwin, Paulo Ceppi, and Giuseppe Zappa (May 2020). “Role of the mean state for the Southern Hemispheric jet stream response to CO₂ forcing in CMIP6 models”. In: *Environmental Research Letters* 15.6, p. 064011. doi: [10.1088/1748-9326/ab8331](https://doi.org/10.1088/1748-9326/ab8331).
- Danabasoglu, G. et al. (2020). “The Community Earth System Model Version 2 (CESM2)”. In: *Journal of Advances in Modeling Earth Systems* 12.2. e2019MS001916 2019MS001916, e2019MS001916. doi: <https://doi.org/10.1029/2019MS001916>.
- Domeisen, Daniela and Amy Butler (Dec. 2020). “Stratospheric drivers of extreme events at the Earth’s surface”. In: *Communications Earth & Environment* 1.59. doi: [10.1038/s43247-020-00060-z](https://doi.org/10.1038/s43247-020-00060-z).
- He, Chengfei, Amy C. Clement, Mark A. Cane, Lisa N. Murphy, Jeremy M. Klavans, and Tyler M. Fenske (2022). “A North Atlantic Warming Hole Without Ocean Circulation”. In: *Geophysical Research Letters* 49.19. e2022GL100420 2022GL100420, e2022GL100420. doi: <https://doi.org/10.1029/2022GL100420>.
- Hurrell, James W. et al. (2013). “The Community Earth System Model: A Framework for Collaborative Research”. In: *Bulletin of the American Meteorological Society* 94.9, pp. 1339–1360. doi: [10.1175/BAMS-D-12-00121.1](https://doi.org/10.1175/BAMS-D-12-00121.1).

- IPCC, Fox-Kemper, B. and Hewitt, H.T. and Xiao, C. and Aðalgeirsdóttir, G. and Drijfhout, S.S. and Edwards, T.L. and Golledge, N.R. and Hemer, M. and Kopp, R.E. and Krinner, G. and Mix, A. and Notz, D. and Nowicki, S. and Nurhati, I.S. and Ruiz, L. and Sallée, J.-B. and Slanger, A.B.A. and Yu, Y. (2021). “Ocean, Cryosphere and Sea Level Change”. In: *Climate Change 2021: The Physical Science Basis. Contribution of Working Group I to the Sixth Assessment Report of the Intergovernmental Panel on Climate Change*. Ed. by V. Masson-Delmotte, P. Zhai, A. Pirani, S. L. Connors, C. Péan, S. Berger, N. Caud, Y. Chen, L. Goldfarb, M. I. Gomis, M. Huang, K. Leitzell, E. Lonnoy, J. B. R. Matthews, T. K. Maycock, T. Waterfield, O. Yelekçi, R. Yu, and B. Zhou. Cambridge, UK and New York, NY, USA: Cambridge University Press. Chap. 9, pp. 1211–1361. doi: [10.1017/9781009157896.011](https://doi.org/10.1017/9781009157896.011).
- Jucker, M., T. Reichler, and D. W. Waugh (2021). “How Frequent Are Antarctic Sudden Stratospheric Warmings in Present and Future Climate?” In: *Geophysical Research Letters* 48.11. e2021GL093215 2021GL093215, e2021GL093215. doi: <https://doi.org/10.1029/2021GL093215>.
- Kidston, Joseph, Adam A Scaife, Steven C Hardiman, Daniel M Mitchell, Neal Butchart, Mark P Baldwin, and Lesley J Gray (2015). “Stratospheric influence on tropospheric jet streams, storm tracks and surface weather”. In: *Nature Geoscience* 8.6, pp. 433–440. doi: <https://doi.org/10.1038/ngeo2424>.
- Kravitz, B., D. G. MacMartin, H. Wang, and P. J. Rasch (2016). “Geoengineering as a design problem”. In: *Earth System Dynamics* 7.2, pp. 469–497. doi: [10.5194/esd-7-469-2016](https://doi.org/10.5194/esd-7-469-2016).
- Kravitz, Ben, Douglas G. MacMartin, Michael J. Mills, Jadwiga H. Richter, Simone Tilmes, Jean-Francois Lamarque, Joseph J. Tribbia, and Francis Vitt (2017). “First Simulations of Designing Stratospheric Sulfate Aerosol Geoengineering to Meet Multiple Simultaneous Climate Objectives”. In: *Journal of Geophysical Research: Atmospheres* 122.23, pp. 12, 616–12, 634. doi: <https://doi.org/10.1002/2017JD026874>.
- Kravitz, Ben, Alan Robock, Olivier Boucher, Hauke Schmidt, Karl E. Taylor, Georgiy Stenchikov, and Michael Schulz (2011). “The Geoengineering Model Intercomparison Project (GeoMIP)”. In: *Atmospheric Science Letters* 12.2, pp. 162–167. doi: <https://doi.org/10.1002/asl.316>.
- Lee, Simon H. (2021). “The stratospheric polar vortex and sudden stratospheric warmings”. In: *Weather* 76.1, pp. 12–13. doi: <https://doi.org/10.1002/wea.3868>.
- Lenton, T. M. and N. E. Vaughan (2009). “The radiative forcing potential of different climate geoengineering options”. In: *Atmospheric Chemistry and Physics* 9.15, pp. 5539–5561. doi: [10.5194/acp-9-5539-2009](https://doi.org/10.5194/acp-9-5539-2009).
- MacMartin, Douglas G., Ben Kravitz, Simone Tilmes, Jadwiga H. Richter, Michael J. Mills, Jean-Francois Lamarque, Joseph J. Tribbia, and Francis Vitt (2017). “The Climate Response to Stratospheric Aerosol Geoengineering Can Be Tailored Using Multiple Injection Locations”. In: *Journal of Geophysical Research: Atmospheres* 122.23, pp. 12, 574–12, 590. doi: <https://doi.org/10.1002/2017JD026868>.
- Mamalakis, Antonios, James T Randerson, Jin-Yi Yu, Michael S Pritchard, Gudrun Magnusdottir, Padhraic Smyth, Paul A Levine, Sungduk Yu, and Efi Foufoula-Georgiou (2021). “Zonally contrasting shifts of the tropical rain belt in response to climate change”. In: *Nature climate change* 11.2, pp. 143–151. doi: <https://doi.org/10.1038/s41558-020-00963-x>.

- Martin, J. E. and T. Norton (2023). “Waviness of the Southern Hemisphere wintertime polar and subtropical jets”. In: *Weather and Climate Dynamics* 4.4, pp. 875–886. doi: [10.5194/wcd-4-875-2023](https://doi.org/10.5194/wcd-4-875-2023).
- McCusker, K. E., D. S. Battisti, and C. M. Bitz (2015). “Inability of stratospheric sulfate aerosol injections to preserve the West Antarctic Ice Sheet”. In: *Geophysical Research Letters* 42.12, pp. 4989–4997. doi: <https://doi.org/10.1002/2015GL064314>.
- Menary, Matthew B and Richard A Wood (2018). “An anatomy of the projected North Atlantic warming hole in CMIP5 models”. In: *Climate Dynamics* 50.7, pp. 3063–3080. doi: <https://doi.org/10.1007/s00382-017-3793-8>.
- NAS, National Academies of Sciences, Engineering, and Medicine (2021). *Reflecting Sunlight: Recommendations for Solar Geoengineering Research and Research Governance*. Washington, DC: The National Academies Press. ISBN: 978-0-309-67605-2. doi: [10.17226/25762](https://doi.org/10.17226/25762).
- Pflüger, D., C. E. Wieners, L. van Kampenhout, R. Wijngaard, and H. A. Dijkstra (2024). “Flawed Emergency Intervention: Slow Ocean Response to Abrupt Stratospheric Aerosol Injection”. In: *ESS Open Archive*. doi: [10.22541/essoar.169447423.32818318/v2](https://doi.org/10.22541/essoar.169447423.32818318/v2).
- Riahi, Keywan, Arnulf Grübler, and Nebojsa Nakicenovic (2007). “Scenarios of long-term socio-economic and environmental development under climate stabilization”. In: *Technological Forecasting and Social Change* 74.7. Greenhouse Gases - Integrated Assessment, pp. 887–935. ISSN: 0040-1625. doi: <https://doi.org/10.1016/j.techfore.2006.05.026>.
- Richter, Jadwiga H., Simone Tilmes, Michael J. Mills, Joseph J. Tribbia, Ben Kravitz, Douglas G. MacMartin, Francis Vitt, and Jean-Francois Lamarque (2017). “Stratospheric Dynamical Response and Ozone Feedbacks in the Presence of SO₂ Injections”. In: *Journal of Geophysical Research: Atmospheres* 122.23, pp. 12, 557–12, 573. doi: <https://doi.org/10.1002/2017JD026912>.
- Robock, Alan (2008). “20 Reasons Why Geoengineering May Be a Bad Idea”. In: *Bulletin of the Atomic Scientists* 64.2, pp. 14–18. doi: [10.2968/064002006](https://doi.org/10.2968/064002006).
- Scambos, T. A., J. A. Bohlander, C. A. Shuman, and P. Skvarca (2004). “Glacier acceleration and thinning after ice shelf collapse in the Larsen B embayment, Antarctica”. In: *Geophysical Research Letters* 31.18. doi: <https://doi.org/10.1029/2004GL020670>.
- Schneider, Tapio, João Teixeira, Christopher S Bretherton, Florent Brient, Kyle G Pressel, Christoph Schär, and A Pier Siebesma (2017). “Climate goals and computing the future of clouds”. In: *Nature Climate Change* 7.1, pp. 3–5.
- Shepherd, J.G. (Sept. 2009). *Geoengineering the climate: science, governance and uncertainty*. Project Report. url: <https://eprints.soton.ac.uk/156647/>.
- Sutter, J, A Jones, TL Frölicher, Christian Wirths, and TF Stocker (2023). “Climate intervention on a high-emissions pathway could delay but not prevent West Antarctic Ice Sheet demise”. In: *Nature Climate Change* 13.9, pp. 951–960. doi: [10.1038/s41558-023-01738-w](https://doi.org/10.1038/s41558-023-01738-w).
- Tilmes, S., D. G. MacMartin, J. T. M. Lenaerts, L. van Kampenhout, L. Muntjewerf, L. Xia, C. S. Harrison, K. M. Krumhardt, M. J. Mills, B. Kravitz, and A. Robock (2020). “Reaching 1.5 and 2.0°C global surface temperature targets using stratospheric aerosol geoengineering”. In: *Earth System Dynamics* 11.3, pp. 579–601. doi: <https://doi.org/10.5194/esd-11-579-2020>.
- Tilmes, Simone, Jadwiga H. Richter, Ben Kravitz, Douglas G. MacMartin, Michael J. Mills, Isla R. Simpson, Anne S. Glanville, John T. Fasullo, Adam S. Phillips, Jean-Francois Lamarque, Joseph Tribbia, Jim Edwards, Sheri Mickelson, and Siddhartha Ghosh (2018). “CESM1(WACCM)

- Stratospheric Aerosol Geoengineering Large Ensemble Project". In: *Bulletin of the American Meteorological Society* 99.11, pp. 2361–2371. doi: [10.1175/BAMS-D-17-0267.1](https://doi.org/10.1175/BAMS-D-17-0267.1).
- UNFCCC, Conference of the Parties serving as the meeting of the Parties to the Paris Agreement (CMA) (Nov. 2023). *Nationally determined contributions under the Paris Agreement. Synthesis report by the secretariat*. URL: [https://eur-lex.europa.eu/legal-content/EN/TXT/?uri=CELEX:22016A1019\(01\)](https://eur-lex.europa.eu/legal-content/EN/TXT/?uri=CELEX:22016A1019(01)).
- Wang, Hai, Shang-Ping Xie, Xiao-Tong Zheng, Yu Kosaka, Yangyang Xu, and Yu-Fan Geng (2020). "Dynamics of Southern Hemisphere Atmospheric Circulation Response to Anthropogenic Aerosol Forcing". In: *Geophysical Research Letters* 47.19. e2020GL089919 2020GL089919, e2020GL089919. doi: <https://doi.org/10.1029/2020GL089919>.
- Wang, Shujie, Hongxing Liu, Richard B. Alley, Kenneth Jezek, Patrick Alexander, Karen E. Alley, Zhengrui Huang, and Lei Wang (2023). "Multidecadal pre- and post-collapse dynamics of the northern Larsen Ice Shelf". In: *Earth and Planetary Science Letters* 609, p. 118077. ISSN: 0012-821X. doi: <https://doi.org/10.1016/j.epsl.2023.118077>.
- Zolotov, S Yu, II Ippolitov, SV Loginov, and EV Kharyutkina (2018). "Variability of the Southern Hemisphere subtropical jet stream in the second half of the 20th century and early 21st century". In: *Izvestiya, Atmospheric and Oceanic Physics* 54, pp. 430–438. doi: <https://doi.org/10.1134/S0001433818050146>.

Code and Data Availability

The CESM2(wACCM6) SSP5-8.5 1.5 data is available at <https://doi.org/10.26024/t49k-1016> from Tilmes et al. (2020).

The CESM2(WACCM6) SSP5-8.5 data was contributed to CMIP6 and is available at <https://esgf-data.dkrz.de/search/cmip6-dkrz/>

The CESM2(CAM6) data for all simulations can be made available upon reasonable request as stated in Pflüger et al. (2024).

All code that was used for analysis and figures can be found at text

A Absolute model differences between CAM and WACCM

The absolute temperature differences between CAM and WACCM for Reference, Control and SAI 2020 are shown in Figure 25. The 2-meter temperature difference reveals that CAM is much warmer than WACCM on the Northern Hemisphere, with the largest difference in the Arctic where the difference exceeds 7° in Reference and SAI 2020. In contrast, CAM is slightly cooler in the Southern Hemisphere, with the difference being generally less than 2°C except for a few areas in Reference.

This difference is lesser in Control, but still a clear difference between the two hemispheres is visible. The difference is worsened in SAI 2020, with the Arctic warming much more in CAM than in WACCM.

As for precipitation, there is a small difference in Reference, with CAM being slightly wetter over the tropics and drier over the western Pacific Ocean. Differences shift in Control, with most notably a stark increase in precipitation over the eastern Pacific Ocean in CAM compared to WACCM. The same is seen in SAI 2020, with the ITCZ also shifting more clearly southward in CAM compared to WACCM.

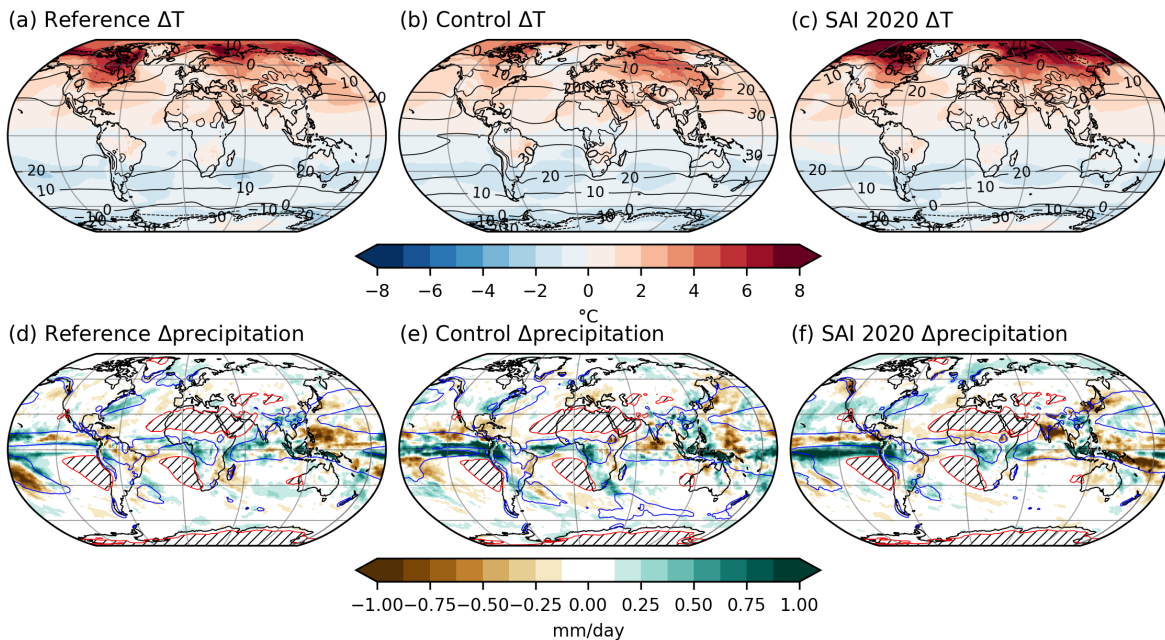


Figure 25: (a-c): Reference, Control and SAI 2020 CAM-WACCM 2-meter temperature differences, WACCM temperature in black contours in 10°C intervals; (d-e): Analogous to (a-c) for precipitation, 4 mm/day in blue contours, < 0.3 mm/day in red contours with hatching.

B Potential Temperature and Zonal Wind JJA

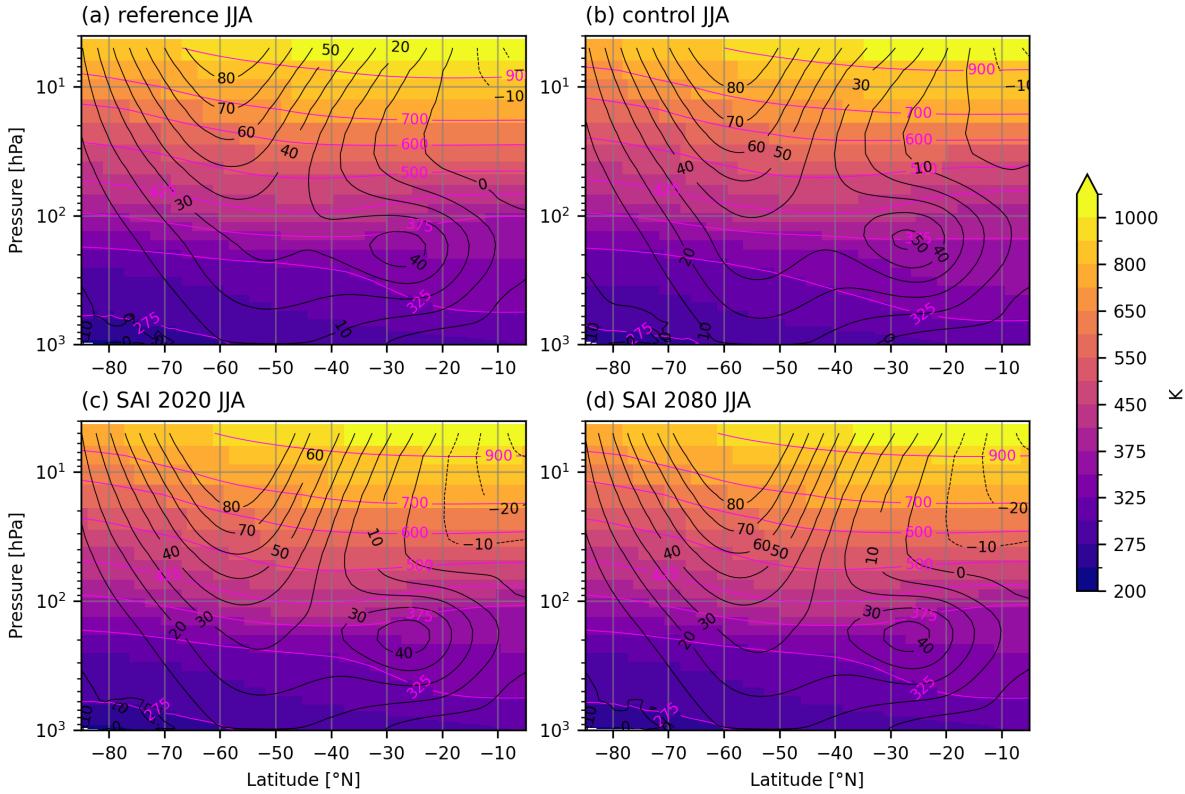


Figure 26: JJA mean zonal-mean potential temperature (shading and magenta contours) and zonal-mean zonal wind (black contours, m/s) for (a) Reference, (b) Control, (c) SAI 2020 and (d) SAI 2080.

C 2-meter Temperature in CAM

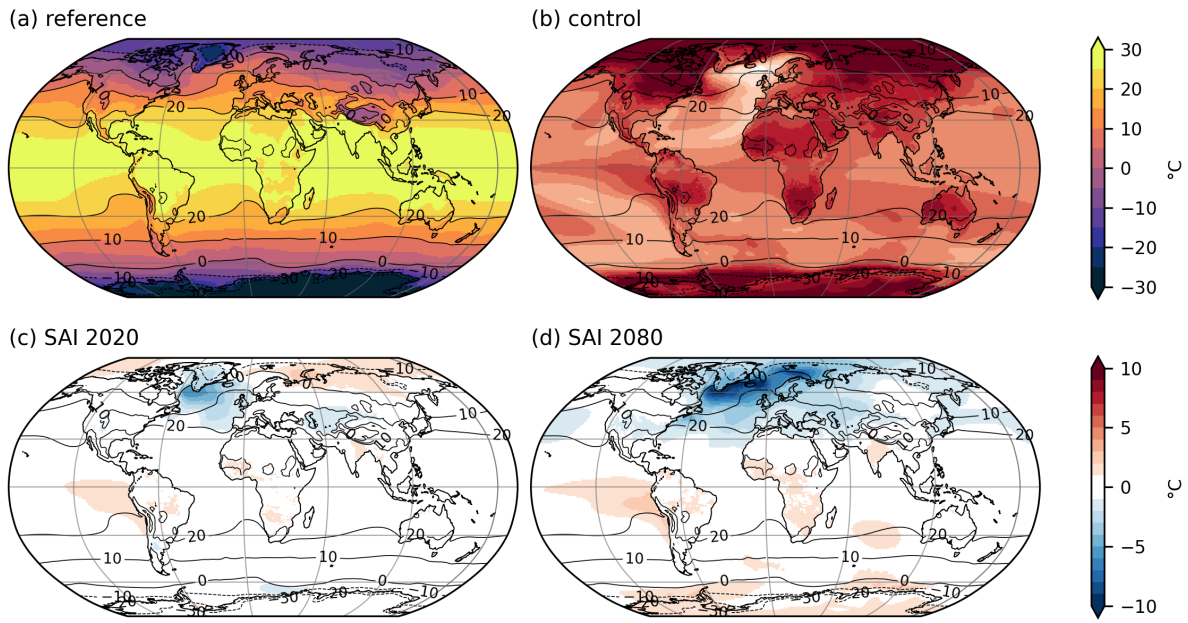


Figure 27: (a): 2-meter tempereature in Reference, contours in intervals of 10°C; (b-d): 2-meter temperature anomaly of (b) Control, (c) SAI 2020 and (d) SAI 2080 compared to Reference, contours as in (a).

D DJF eddy kinetic energy and Eddy Driven Jet Position

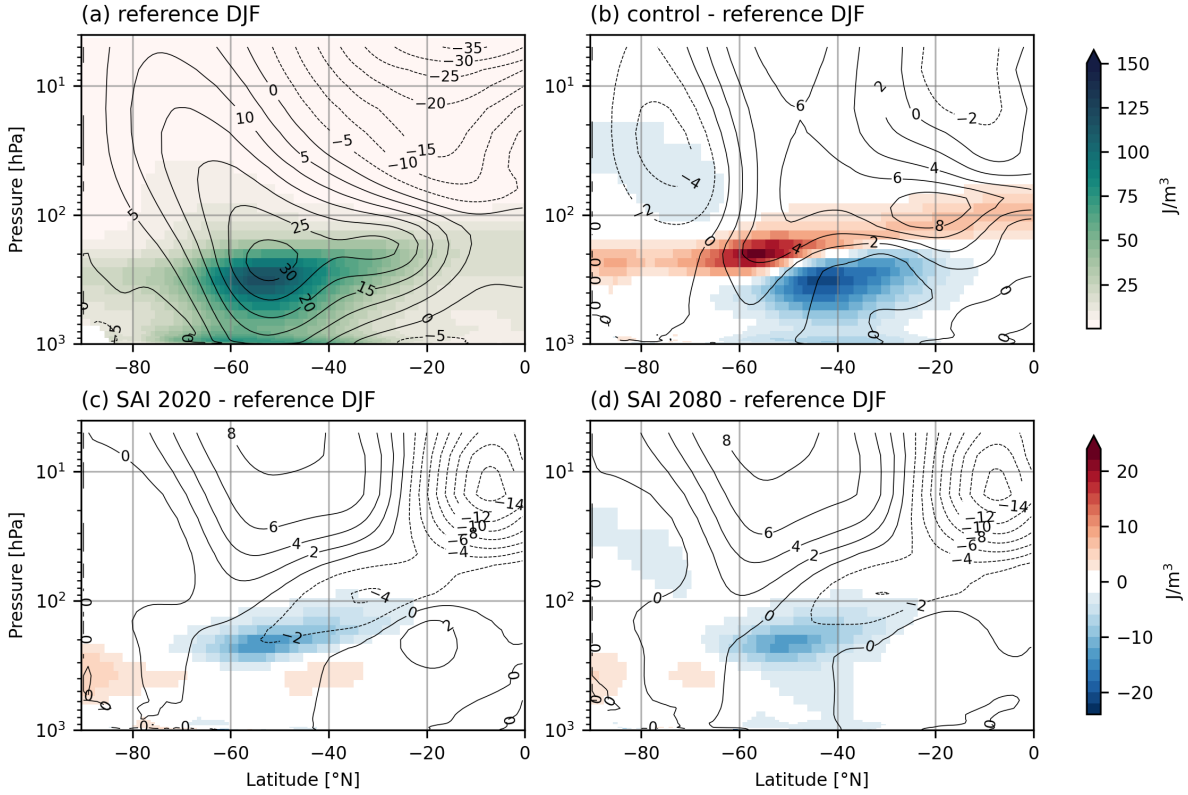


Figure 28: DJF mean zonal-mean eddy kinetic energy (shading) and zonal-mean zonal wind (contours, m/s) for (a): Reference; (b-d): Control, SAI 2020 and SAI 2080 anomaly compared to Reference.

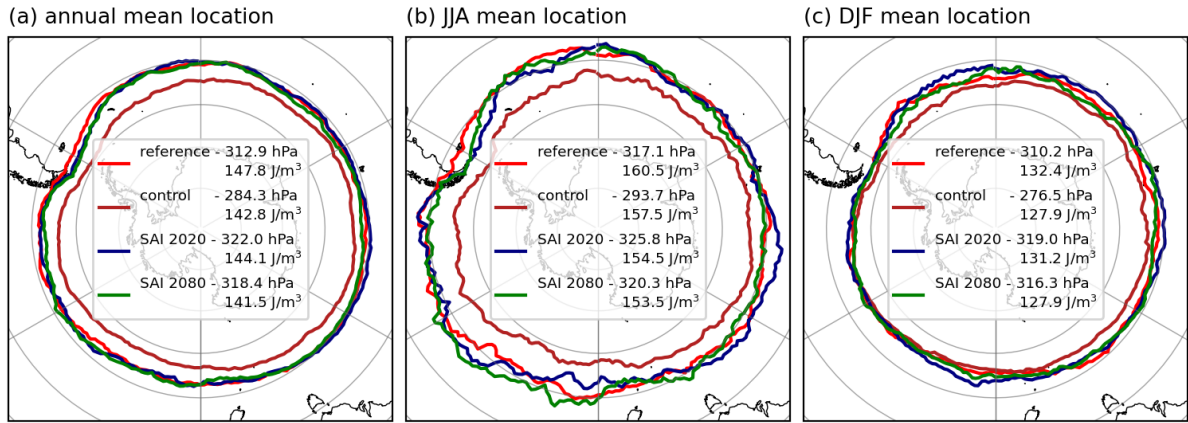


Figure 29: Mean location of the maximum of the subtropical jet, with corresponding longitudinal mean height and maximum eddy kinetic energy for Reference, Control, SAI 2020 and SAI 2080 for the (a) annual mean, (b) JJA mean and (c) DJF mean. 0°E is oriented towards the top of the figure.